THE UNIVERSITY OF
WARWICK

Modeling the evolution of natural cliffs subject to weathering: 1. Limit analysis approach

S. Utili[1] and G. B. Crosta[2]

[1]   Retrogressive landsliding evolution of natural slopes subjected to weathering has been modeled by assuming Mohr-Coulomb material behavior and by using an analytical method. The case of weathering-limited slope conditions, with complete erosion of the accumulated debris, has been modeled. The limit analysis upper-bound method is used to study slope instability induced by a homogeneous decrease of material strength in space and time. The only assumption required in the model concerns the degree of weathering within the slope, and for this we assumed and tested different weathering laws. By means of this method, the evolution of cliffs subject to strong weathering conditions (weathering-limited conditions) was predicted. The discrete succession of failures taking place was modeled taking into account the geometry assumed by slopes as a consequence of previous mass movements. The results have been compared with published data from long-term slope monitoring and show a good match between experimental observations and analytical predictions. The retrogressive evolution of the slope occurs with decreasing size of the unstable blocks, following a logarithmic volume-frequency relationship. A nonlinear relationship is found between mass flux and average slope gradient. A set of normalized solutions is presented both by nomograms and tables for different values of slope angle, cohesion, and internal friction angle.

1.   Introduction

[2]   Slope evolution has been described through different approaches based on direct observations and assumptions concerning the volume of sediment released from uphill and passing through a specific length of the profile. On this basis, transport laws have been proposed and implemented in landscape evolution models of the process-response type. Transport-limited and weathering-limited conditions [*Kirkby*, 1971] have been considered. In the first case, the transport processes have a complete availability of material and, consequently, their intensity and spatial distribution control slope evolution. Conditions of this type can be associated with slopes where landslides play a relevant role in debris supply. On the other hand, weathering-limited (or detachment-limited) conditions are those where a limited amount of material is made available for full activation of transport processes by various mechanisms (e.g., physical and chemical weathering).

[3]   Among the proposed models, some of them are not directly linked to time and others explicitly include the effect of time. The earliest efforts [*Fisher*, 1866; *Lehmann*, 1933; *Bakker and Le Heux*, 1946, 1952] were mainly focused on the evolution of vertical or constant angle cliffs associated (or not) with the development of a talus slope. Subsequently, diffusion equation concepts have been applied to hillslope erosion modeling [*Scheidegger*, 1961; *Culling*, 1963; *Ahnert*, 1970a, 1970b, 1970c; *Kirkby*, 1971; *Carson and Kirkby*, 1972; *Nash*, 1980a, 1980b; *Pierce and Colman*, 1986; *Fernandes and Dietrich*, 1997; *Pelletier et al.*, 2006] considering the action of one or more quasi-continuous processes (e.g., creep, washing, rain splash, shallow landsliding, and mass movements) [*Nash*, 1980a, 1980b; *Colman and Watson*, 1983; *Hanks et al.*, 1984; *Andrews and Bucknam*, 1987; *Anderson and Humphrey*, 1989; *Howard*, 1994; *Roering et al.*, 1999, 2001a, 2001b; *Martin and Church*, 1997, 2004].

[4]   In all these cases the general slope evolution is controlled by assumptions concerning debris accumulation, the bulking of the material, the geometry of the failing blocks, the coefficient of diffusivity, the weathering and crest regression rate, the linear and nonlinear dependency of sediment flux on slope gradient. Furthermore, no mechanical properties are considered in such models with the exception of a few studies [e.g., *Andrews and Bucknam*, 1987].

[5]   The aim of this study is to present an analytical solution able to demonstrate the physical and mechanical link between observations and material behavior. The approach is developed for a weathering-limited slope condition where landslide material is carried away from the slope toe, leaving it completely exposed. The slopes studied are all steeper than the internal friction angle characteristic of the forming

---

[1]Department of Engineering Science, University of Oxford, Oxford, UK.
[2]Dipartimento di Scienze Geologiche e Geotecnologie, Università degli Studi di Milano-Bicocca, Milan, Italy.

material. Landsliding is considered as deep seated unlike the usual approaches typically involving shallow failures [*Martin and Church*, 1997; *Martin*, 2000]. This difference partially implies that the analyzed phenomena can be considered as episodic [*Koons*, 1989; *Willgoose et al.*, 1991; *Chase*, 1992; *Kooi and Beaumont*, 1994] with respect to shallow landsliding which is often considered as continuous. Nevertheless, discrete or quasi-continuous landsliding events could occur while continuous processes act. As a consequence, in these cases the transport law and the slope erosion can be more complicated than are usually considered. Until now, only very basic models have been used to analyze slope evolution by landsliding. Empirical and semiempirical methods have been adopted to support geomorphic transport laws for such a class of processes, and this manuscript attempts to contribute to this aspect.

[6] The limit analysis approach is applied for a range of values of slope inclination and of the material strength parameters (cohesion and internal friction angle), describing the behavior of a homogeneous material under uniformly distributed weathering. Eventually, the changes in sediment flux with time are examined together with the dependence on average slope gradient.

2. Behavior of Geomaterials

[7] In general, it can be said that slope failure is controlled either by a decrease in the strength of the material or by an increase in the forces acting. For the problem analyzed in this paper, a decrease in strength is assumed to be the controlling factor. As a consequence, it is relevant to discuss some aspects of the strength of geomaterials and their degradation

[8] In Figure 1a, the failure envelopes obtained from tests on a granitic rock subject to various degrees of weathering are shown [*Kimmance*, 1988]. The failure loci are well approximated by straight lines which are characterized by the intercept with the ordinate axis (i.e., cohesion) and their inclination (i.e., friction angle). From Figure 1 it is apparent that weathering causes a reduction mainly of cohesion and to a much lesser extent of the friction angle. The same considerations apply for hard soils like the cemented sand shown in Figure 1b [*Wang and Leung*, 2008]. In this case, the failure envelopes have been achieved from triaxial tests run for different contents of cement. This type of geomaterial is prone to the occurrence of chemical reactions which progressively dissolve the cement bonds holding together the sandy/silty grains. This reduces the amount of cement, which can be uniquely related to a known degree of weathering, varying from zero for the initially cemented material to 100% for completely debonded grains.

[9] Similar considerations apply to many materials as shown by *Leroueil and Vaughan* [1990] for a large variety of overconsolidated clays and structured soils. This experimental evidence justifies, as a first approximation, the assumption that weathering causes mainly a decrease of cohesion, and to a much lesser extent of the friction angle. In the paper, first the case of a cohesion-only decrease is tackled (see Figure 1c), then a refined modeling for the case of both cohesion and friction decrease is undertaken (see Figure 1d). In both cases, slopes are assumed to be homogeneous. This assumption represents an oversimplification of reality, since weathering

has a greater effect on material close to the exposed surface than on material well within the slope. As a matter of fact, from the scanty experimental data available [*Yokota and Iwamatsu*, 2000; *Hachinohe et al.*, 2000], it can be inferred that soil strength varies between the exposed slope forefront, where it is minimal, up to an internal weathering propagation front, to remain constant within inner slope regions (see Figure 2). Unfortunately, such a spatial variation cannot be taken into account easily by an analytical approach, as the limit analysis method requires very complex calculations already for the case of uniform weathering. The assumption of uniform weathering, although unrealistic, allows quick generation of tables and charts of results (see auxiliary material) which give a first rough estimate of the evolution of a slope.[1] This could be investigated by a more refined but time-consuming model (e.g., the discrete element method (DEM)) capable of taking into account the spatial variation of weathering intensity [see *Utili and Crosta*, 2011; *Utili and Nova*, 2008]. Moreover, the critical values of c, ϕ achieved for each landslide event can be thought as a spatial average of the local c, ϕ values varying within the slope.

## 3. Limit Analysis Upper-Bound Predictions

3.1. Introduction

[10] The limit analysis upper-bound method has been adopted in this analysis to study the profiles assumed by a slope with uniform c (cohesion) and ϕ (internal friction angle) distributions and subject to spatially uniform degradation. Upper bounds on the collapse values associated with a series of successive profiles have been determined. Each subsequent landslide is assumed to be characterized by a rigid rotational mechanism (see Figure 3a) with energy being dissipated along the failure surface between a sliding rigid block and the remaining material at rest.

[11] The limit analysis method assumes the validity of the normality rule, that is, associated plastic flow, which does not hold true for either rocks or clayey soils. Nevertheless, it is known [*Radenkovic*, 1961] that an upper-bound value of the safety factor, calculated by assuming the validity of the normality rule, is also an upper bound for a material with the same strength parameters but a dilation angle (Ψ) less than friction angle (nonassociated flow rule). Concerning the failure criterion, it is assumed that the normal and shear stresses along the slip surface obey the Mohr-Coulomb criterion (see Figure 1). This is the most used criterion for slope stability problems in cohesive soils.

[12] It is worth pointing out that from a theoretical point of view, the most critical surface is not given by a single rotating block mechanism. For instance, if multiple rotation mechanisms are adopted, the upper-bound solution obtained is slightly lower, but this improvement is negligible to our aim. For instance, *Bekaert* [1995] found a mere 1.0% increase on the maximum height of a vertical cut in a Tresca material ($\phi = 0$), by considering a multiple rotation mechanism made up of n log spiral shaped rigid blocks instead of a single one. Furthermore, the numerical lower-bound results obtained by *Lyamin and Sloan* [2002] are only 1.8%
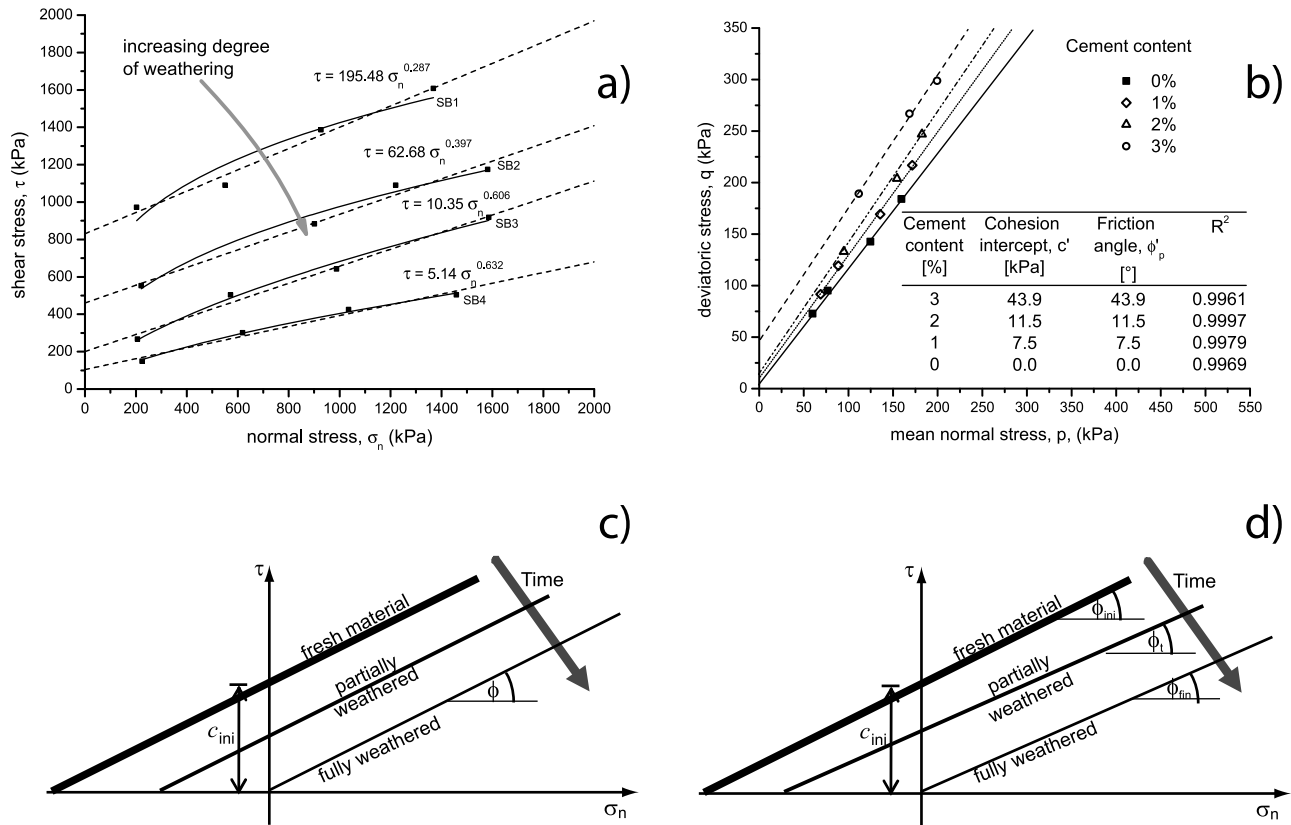
Figure 1. (a) Weathering of granite [after *Kimmance*, 1988], (b) failure loci of cemented sands for different cement contents [after *Wang and Leung*, 2008], (c) failure criterion evolution in case of cohesion only decrease, and (d) failure criterion evolution in case of both cohesion and friction decrease.

less than the calculated upper bound for $\phi = 0$ analyses, and the difference between lower and upper bounds is even smaller when $\phi > 0$, as in the cases analyzed here. This very small error in approximating the true collapse value is negligible in comparison with much higher uncertainties in relation to the in situ determination of ϕ, c values and to the weathering law. Therefore, for all practical purposes, the values determined by the assumed single rotational mechanisms can be considered as accurate theoretical collapse values.

[13] Our analysis is based on the assumption, which does not derive directly from limit analysis, that the velocity field associated with the lowest-limit load for a rotational mechanism is a reasonable approximation of the actual field, and its logarithmic spiral boundary is assumed to represent the failure line forming in the deteriorating slope. But, the kinematic method of limit analysis does not give any information on the actual field of velocities or its relation to the field considered. No conclusion can be drawn as whether the failure line associated with the lowest-limit load is outside, inside, or somewhere else with respect to the true line. An example of physically incorrect velocity field for a cohesive material is demonstrated by *Shield and Drucker* [1953], and for a frictional/cohesive material by *Zhu and Michalowski* [2005], both dealing with square punch indentation. Actually, it is not possible to rigorously quantify the error introduced by this approximation since there is no correlation between the known error on the limit load (i.e., how far the upper bound is from the true collapse load), and the unknown error on the velocity field (i.e., how far the

velocity field of the rigid rotational mechanism associated with the upper bound is from the real velocity field associated with the true collapse load). In other words we cannot quantify the extent to which the approximation on the
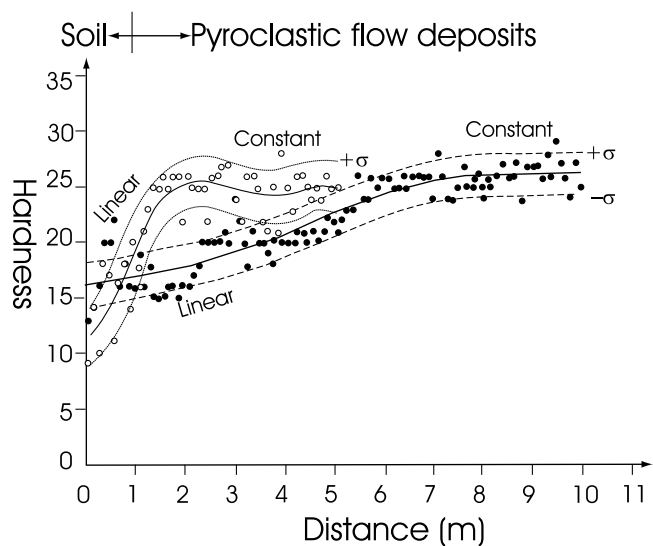

Figure 2. Hardness distributions obtained from the top of the slope (solid circles) and the foot of the slope (open circles). In both cases a bilinear spatial variation of hardness can be observed [after *Yokota and Iwamatsu*, 2000].
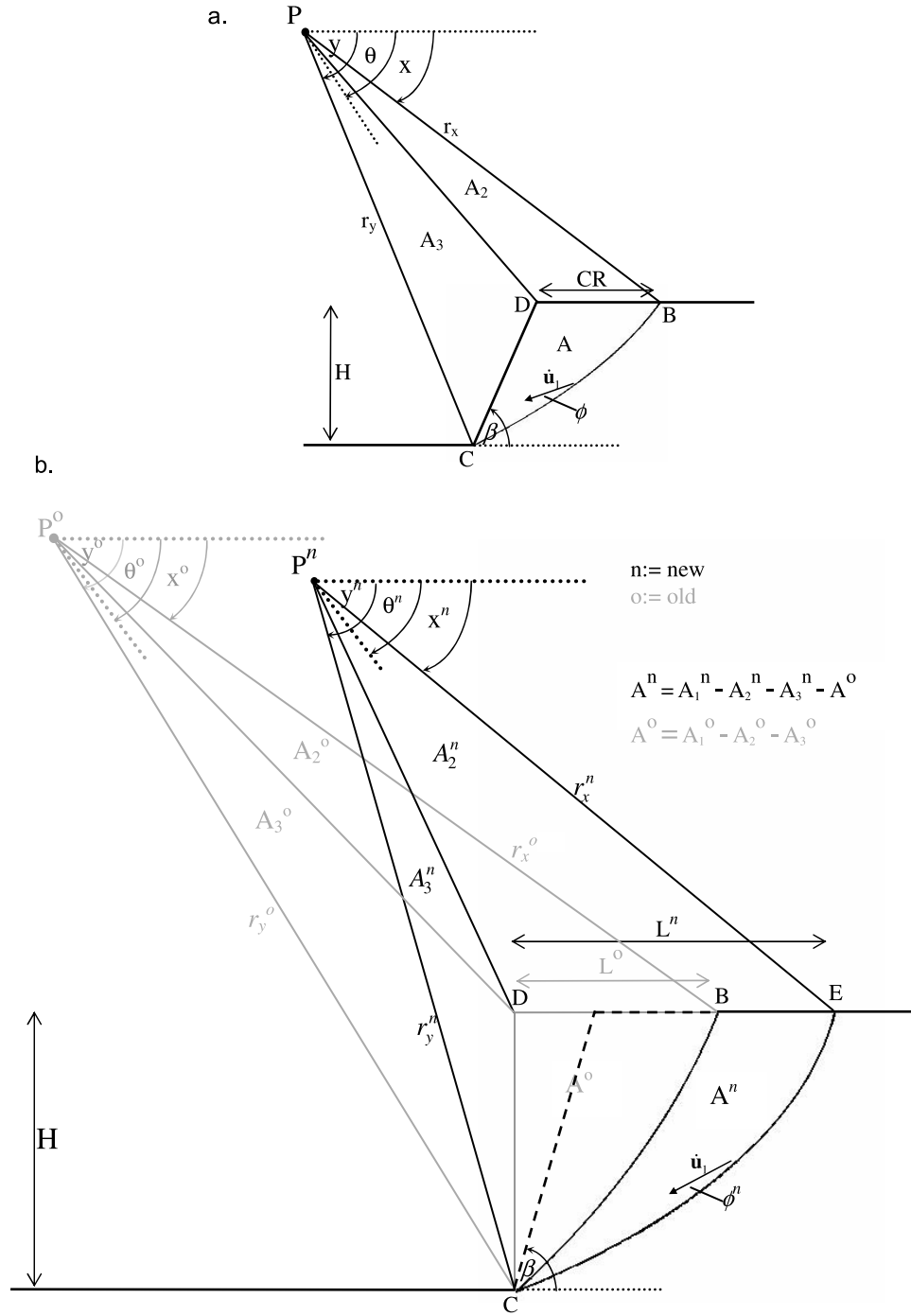
Figure 3. (a) First failure mechanism and (b) second failure mechanism. Gray lines are relative to the old spiral (B-C) whereas black lines to the new one (E-C). Dashed lines indicate the initial slope profile before first failure occurrence.

assumed velocity field affects the estimate of the limit load of the subsequent failure mechanisms. However, with regard to the first landslide, recent plane strain finite element analyses of homogeneous slopes by the shear strength reduction technique assuming the validity of the normality rule ($\Psi = \phi$), as postulated in limit analysis, show that the shape of the failure line is a logarithmic spiral [*Dawson et al.*, 1999; *Zheng et al.*, 2005].

[14] An alternative formulation to the limit analysis upper-bound method based on the limit equilibrium method, which is in general more familiar to practitioners, could be employed as well. In the work by *Utili* [2006], the limit equilibrium formulation is presented in detail and it is shown that the equilibrium of moments for the detaching material together with the Mohr-Coulomb failure criterion, lead to the analytical functions of equations (3) and (4).
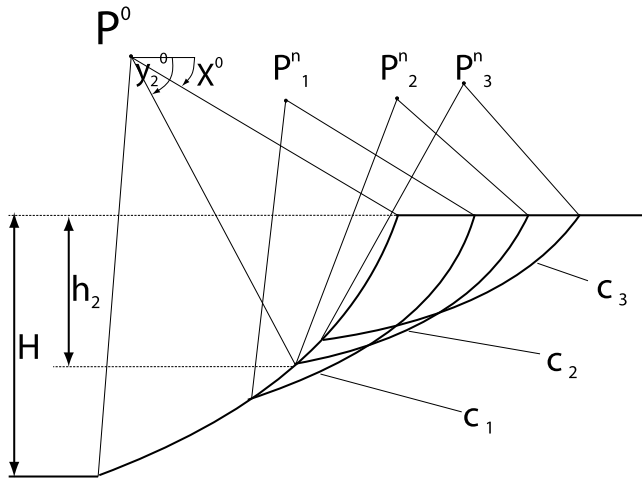
Figure 4. Failure lines relative to the different mechanisms considered.

In this paper, the limit analysis upper-bound method has been preferred since it provides rigorous upper-bound values as discussed above.

[15] As already pointed out, cliff weathering is likely to cause a decrease of both friction angle and cohesion, with cohesion being the parameter most affected by degradation. For the sake of clarity, first the case of only decreasing cohesion will be illustrated in section 3.3 [see also *Utili*, 2005]; then the case of decreasing ϕ and c will be introduced in section 3.5. In the following, the calculations will be illustrated for the case of a horizontal slope crest, $\alpha = 0$ (see Figure 3), whereas the case of a nonhorizontal slope crest, $\alpha \neq 0$ (see Figure A1), will be examined in the Appendix only.

[16] Finally, it is also worth noting that the material accumulated at the slope toe cannot be taken into account in our model since the limit analysis method is not able to give any information about the final geometry of the debris accumulated after each landslide. Therefore, in this model, it is assumed that the debris accumulating at the slope toe is removed by atmospheric agents or fluvial or marine erosion, before a new landslide develops. This condition is known in the literature as a strong erosion condition and is typical of weathering-limited processes [*Hutchinson*, 1973]. The effect of talus formation at the slope toe will be examined by DEM modeling in the companion paper by *Utili and Crosta* [2011].

3.2. Limit Analysis Model

3.2.1. First Failure Mechanism

[17] According to the assumed failure mechanism, the logarithmic spiral–shaped region D-B-C (Figure 3a) rigidly rotates about a center of rotation P, as yet undefined, with the material below the logarithmic spiral surface B-C remaining at rest. This mechanism is completely defined by two variables, which in the literature are usually taken as the maximum and minimum angles (x and y in Figure 3) of the logarithmic spiral. The stability number, N_S, defined as $N_S = \gamma H/c$, is a convenient measure of the stability of a homogeneous slope with height H, inclination β and soil of unit weight γ (soil weight per unit of volume), and strength given by c and ϕ. The analytical expression for the stability number is obtained by calculating the rate of external work

($\dot{W}_{ext}$) done by the region of material slipping away and by the dissipated energy ($\dot{W}_{dis}$) along the failure line, then equating the two:

$$\dot{W}_{ext} = \dot{W}_{dis}. \tag{1}$$

In order to find the most critical mechanism among all the kinematically admissible ones, the minimum value of the function obtained by equation (1) must be taken, so that the stability number is

$$N_S = \min_{x,y} f(x, y, \beta, \phi). \tag{2}$$

The full analytical expression of $f(x, y, \beta, \phi)$ can be found in the work by *Chen* [1975]. In our case, cohesion and friction are uniformly decreasing with time throughout the slope because of weathering, and the value at the occurrence of the first landslide is sought. When this takes place, the factor of safety is equal to 1 and the critical value of cohesion is obtained from the inverse of the stability number:

$$c^1 = \gamma H \frac{1}{\min_{x^1 y^1} f(x^1, y^1, \beta, \phi^1)} = \frac{\gamma H}{N_S^1}. \tag{3}$$

In equation (3) the superscript 1 indicates that the c, ϕ values refer to the occurrence of the first failure.

[18] Knowing the relationship between time (t), decrease of strength (decrease of c, ϕ), and initial strength (c^{ini}, ϕ^{ini}), it is possible to predict the time t_1 of the occurrence of the first failure. Weathering laws relating soil strength to time will be introduced in section 3.4. In this section and in section 3.3, the succession of failure mechanisms will be determined assuming that c and ϕ decrease over time without assuming any weathering law. This can be introduced subsequently to determine the times, t_i, of occurrence of each landslide of the sequence.
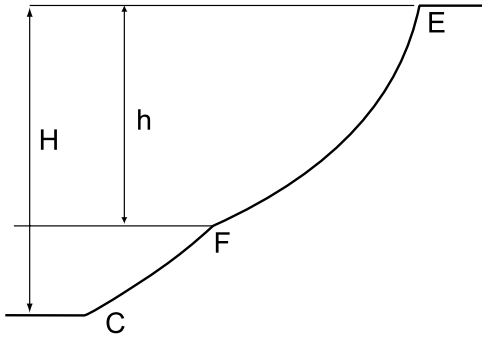
3.2.2. Second Failure Mechanism

[19] After the logarithmic spiral shaped region D-B-C has slipped away, the slope profile is characterized by a logarithmic spiral geometry (Figure 3b). Because of further weathering, at a certain time t_2, a second landslide occurs. In this case the double logarithmic spiral shaped region B-C-E will rigidly rotate about a center of rotation P^n, as yet undefined, with the material below the logarithmic surface C-E remaining at rest (see Figure 3b). Proceeding as before, the value of cohesion associated with the second failure is found:

$$c^2 = \gamma H \frac{1}{\min_{x^2, y^2} g(x^2, y^2, \phi^2, x^1, y^1, \phi^1)}, \tag{4}$$

where x^2, y^2 are the angles defining the second log spiral failure line (see Figure 3b); x^1, y^1 are the angles defining the first log spiral failure line (i.e., the current slope profile produced by the previous failure); and ϕ^2 is the current friction angle of the slope, whereas ϕ^1 is the value of ϕ at the occurrence of the first slide. Details of the lengthy analytical calculations leading to the g function are reported in Appendix A2.

[20] So far, it has been implicitly assumed that the new logarithmic spiral failure surface passes through the slope toe (see Figure 3b). In fact, the failure surface passes below the toe only for very low friction angles, $\phi \leq 5°$ [see *Taylor*, 1948; *Michalowski*, 2002], which are well below physically

Figure 5. Slope profile after the third failure.

meaningful values for dry/drained conditions. This second mechanism could pass above the slope toe since the current slope profile is no longer straight. To take this possibility into account, the spiral slope has been divided into a discrete number of points (n) and each point has been assumed as the toe of a slope whose height, h_i, is lower than the overall height, H (Figure 4). Analyses with different values of n were run; if n is chosen as $n \geq 2000$ accurate results are

obtained for any value of ϕ and β. The critical cohesion values, c_i, and angles, x_i and y_i, associated with the critical log spiral, have been determined for all n slopes of different height, h_i, minimizing $g = g(x^2, y^2, \phi^2, x^1, y_i^1, \phi^1)$ where the parameter y_i^1 assumes a different value associated with each "subslope". The most critical failure mechanism among the n potential mechanisms is the one with the highest cohesion value.

3.2.3. Successive Failure Mechanisms

[21] In order to determine the third failure surface, the same procedure used to find the second one is adopted. Equation (4) modifies into

$$c^i = \gamma H \frac{1}{\min_{x^i, y^i} g(x^i, y^i, \phi^i, x^{i-1}, y^{i-1}, \phi^{i-1})}. \tag{5}$$

The obtained results have shown that the third failure mechanism passes above the slope toe for any initial inclination β of the slope with $90° \geq \beta > \phi$ and $\alpha = 0$.

[22] After the third failure, the slope geometry is characterized by a boundary made of two logarithmic spirals (see Figure 5). This makes it no longer possible to apply the same procedure in order to determine the subsequent fourth
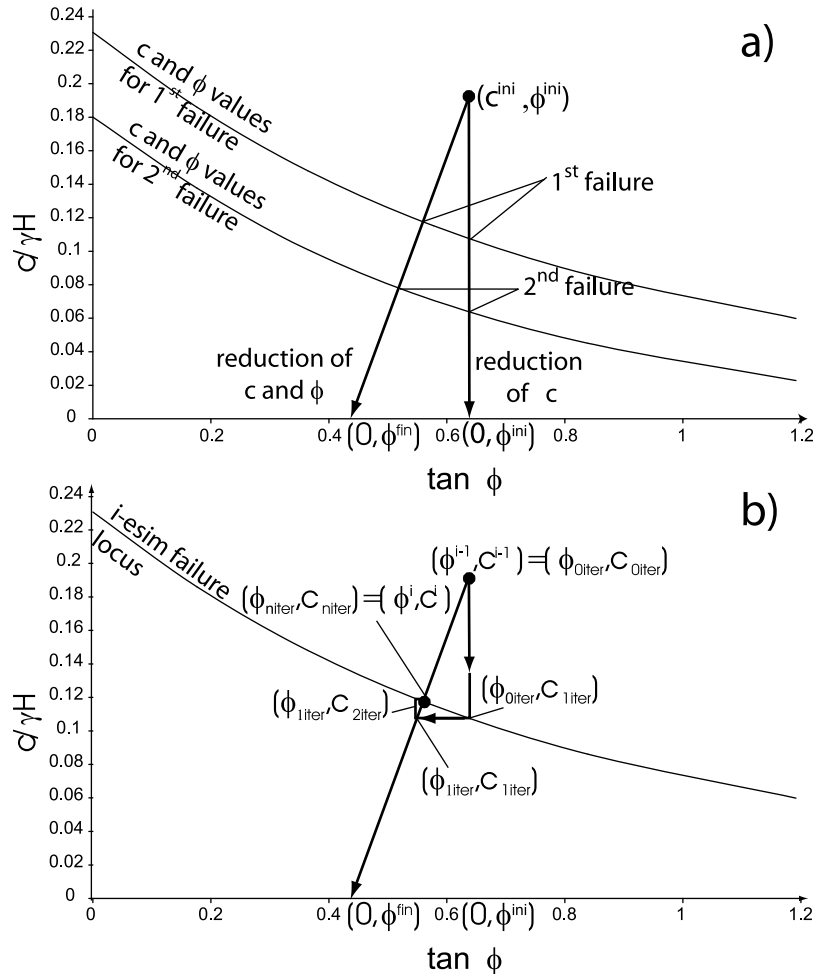
Figure 6. (a) Graphical representation of the reduction of c, ϕ applied throughout the cliff. In order to determine the values of c, ϕ at failure, an iterative procedure is used each time. (b) Graphical representation of the algorithm used in Matlab to find c, ϕ for each successive failure.
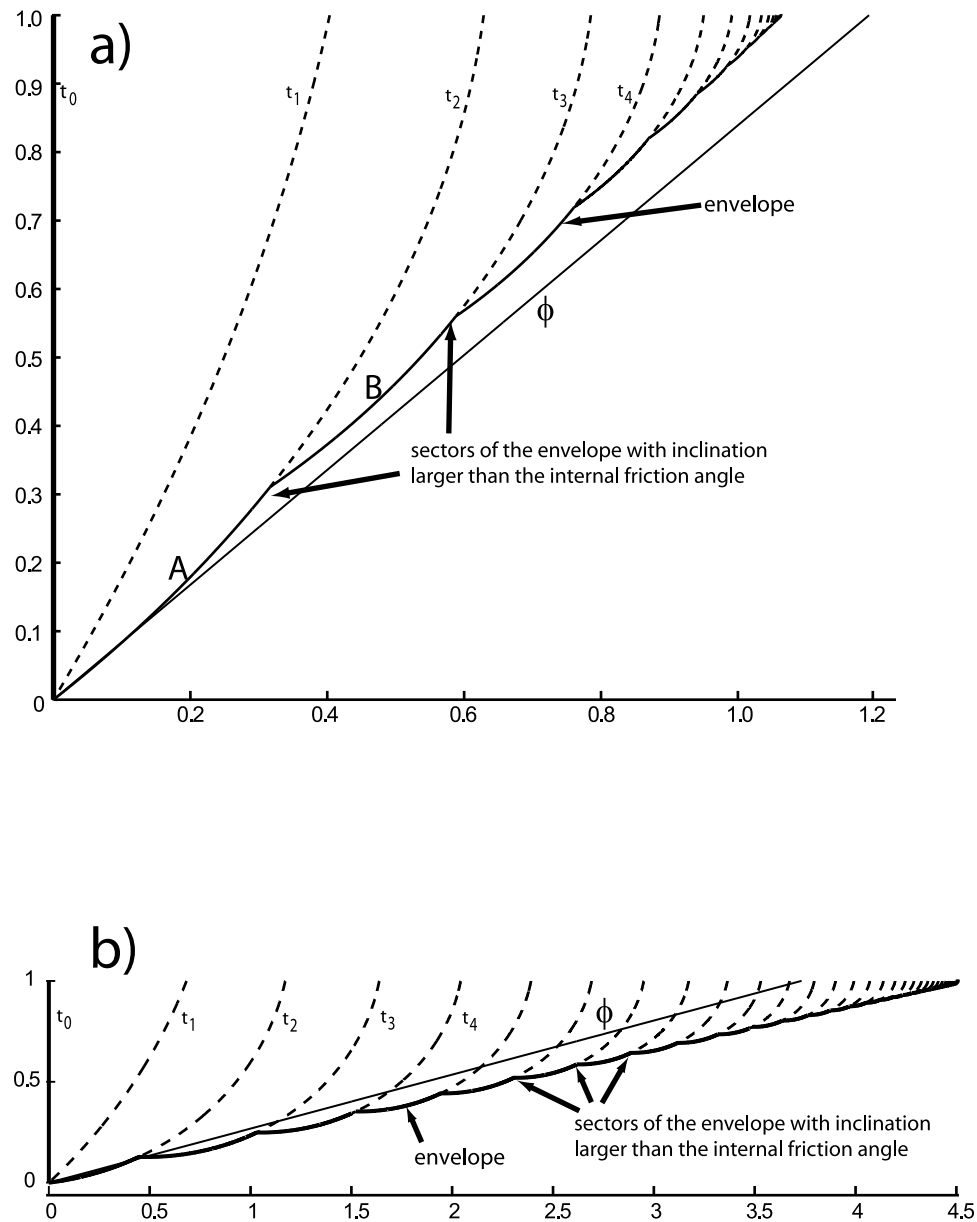
Figure 7. Slopes are initially vertical (solid line) and subject to uniform cohesion decrease. The subsequent profiles at times t_i are shown by dashed log spiral lines. The final profile at t_{fin} is given by a log spiral piecewise solid curve. (a) Constant friction $\phi = 40°$ and (b) constant friction $\phi = 15°$. The slope height is normalized to 1.

failure. A slope profile made by two spiral pieces requires four parameters for its complete description, and the calculation of the external work done by the sliding soil mass would require the calculation of the area and location of the center of gravity of a region enclosed by three log spiral pieces (i.e., two for the outer slope profile and one for the failure surface). This makes the analytical equations involved in the energy balance far more complicated. To find the fourth mechanism, the potential failure lines have been initially sought only above the point of intersection of the two spirals making up the current slope profile (point F in Figure 5), applying the procedure to ascertain the most critical failure mechanism with respect to the upper-spiral profile only. Since in all the cases analyzed, the failure line

associated with the highest cohesion value was always found to pass above the toe of the upper spiral, this implies that the failure line does actually pass above point F.

[23] Applying this procedure, it is possible to determine as many failure mechanisms as needed to follow the slope evolution until full degradation of the soil strength is reached. Strength degradation has been considered to end at $c = 0$ in case of $\phi = \phi^{const}$; whereas in case of both c and ϕ decreasing, full degradation is reached at $c = 0$ and $\phi = \phi^{fin}$ (final friction angle). A graphical representation of the two scenarios of weathering is illustrated in Figure 6a where straight lines represent the progressive decrease of mechanical strength, and curved lines represent the loci of c, ϕ values for the first and second landslide obtained by
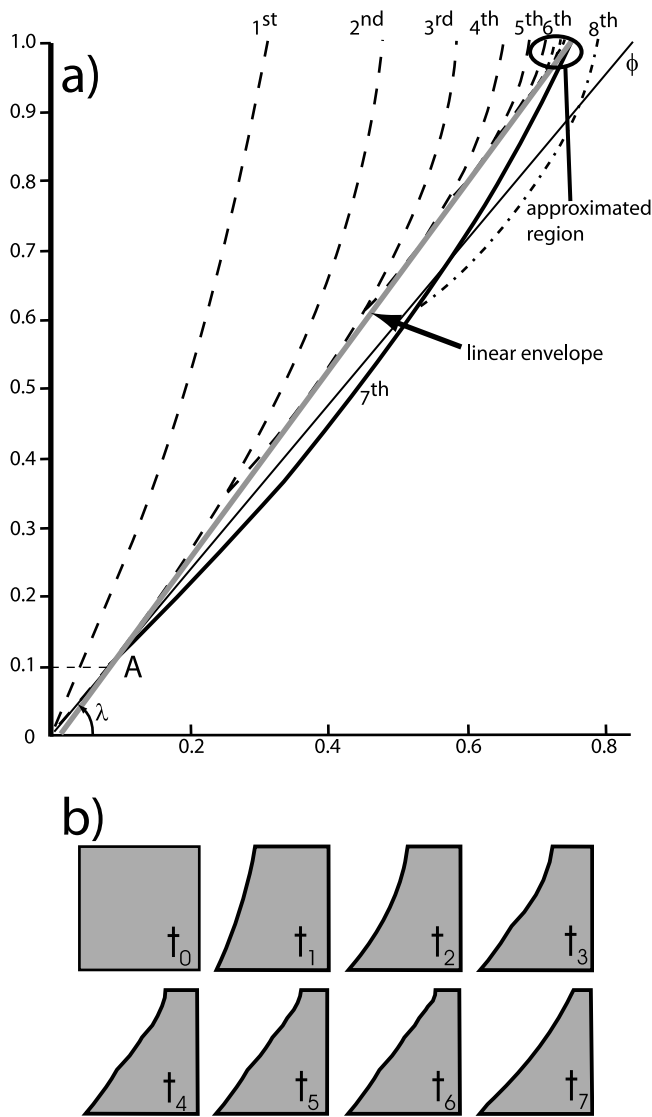
Figure 8. Initially vertical slope (solid line) subject to uniform cohesion decrease with $\phi = 50°$. Dashed lines represent the subsequent log spiral landslide profiles. The straight gray line envelopes the achieved log spiral piecewise slope profile. The solid thick log spiral line (t_7) refers to the seventh mechanism. The subsequent mechanism (t_8) is represented by a dash-dotted log spiral line. The thin line represents the friction angle ϕ. The slope height is normalized to 1.

parametric analyses run for different values of c and ϕ. The intersections of the straight lines with the loci give the values of c, ϕ associated with the first two landslides for the different weathering scenarios considered.

3.3. Pure Cohesion Decrease

[24] As a first approximation, as discussed above, it is reasonable to assume that weathering only affects cohesion, with ϕ remaining constant. This hypothesis on weathering can be visualized in the $c/\gamma H$-ϕ plane shown in Figure 6 by the path along the vertical straight line. Assuming that only cohesion decreases, the friction angles used in the optimization processes for each mechanism are all the same,

therefore $\phi = \phi^1 = \phi^2 = \dots = \phi^m$, with m being the last mechanism considered; therefore $g = g(x^i, y^i, x^{i-1}, y^{i-1}, \phi)$. The condition $c = 0$ can only be rigorously reached after an infinite number of mechanisms take place, but a finite number m of mechanisms, so that $c^m \sim 0$, is enough to catch the full evolution of the slope for practical purposes. The number m of mechanisms considered depends on ϕ: the lower ϕ is, the higher m needs to be.

[25] The full evolution of an initially vertical slope ($\beta = 90°$) is shown in Figure 7 for two different values of friction angle: $\phi = 40°$ and $\phi = 15°$. It is now necessary to look at the final condition in order to assess if it is physically sound. In the final state the material is purely frictional ($\phi = const$, $c^m \sim 0$) and therefore the inclination of the local tangent to any point along the final profile (solid line in Figure 7) must be lower than ϕ for the profile to be stable (i.e., a purely frictional material cannot withstand slopes larger than the friction angle). The final profile is made up of several segments of log spirals which in their upper parts (see Figure 7) are characterized by a local inclination higher than ϕ. Several "secondary" processes (e.g., shallow landslides, creep, etc.) must take place before the cohesion decreases to zero where the local inclination of the profile is higher than ϕ. After some main failures have occurred, we expect that "secondary" failures start. The first failure to occur lies between points A and B (see Figure 7) for a value of cohesion much lower than the values for which the first deep failure mechanisms take place. With cohesion decreasing further, a series of successive secondary shallow failures take place. Fortunately, these small movements do not affect the rate of retreat of the crest and it is reasonable to assume that their only effect is to smooth the profile solely within those regions where the local inclination is higher than ϕ.

[26] In order to know if the profile for fully weathered conditions, $c \rightarrow 0$, is globally stable the final profile (solid line in Figure 7) has been approximated by a straight line enveloping all the log spiral segments making the profile. In this way the occurrence of secondary failures smoothing the profile over its many kink points is taken into account. The inclination of this line, λ, is larger than ϕ for friction values larger than 22° (Figure 7a), and smaller than ϕ for friction values below 22° (Figure 7b).

[27] In case of $\lambda < \phi$, the final profile is stable, and the log spiral piecewise solid line represents the final profile except for the occurrence of the secondary mechanisms discussed above. As mentioned above, it is not possible to calculate these mechanisms, but it is reasonable to suppose that successive small failures will eventually make the slope profile planar, as suggested by experimental observations [*Hutchinson*, 1973].

[28] On the contrary, in case of $\lambda > \phi$, this condition cannot be the final one. In fact, a plane inclined at an angle larger than ϕ cannot be stable at $c = 0$. This result may be explained through the procedure used to determine each successive "primary" landslide. After each failure, the next one is sought in the region to the right of the last log spiral (between points E and F in Figure 5), disregarding the possibility of failures below the last spiral (points C and D in Figure 5). This choice is justified by the fact that the most critical line found at the end of the optimization process was always passing well above the toe of the last log spiral. Nevertheless, after the occurrence of a certain number of

Table 1. Values of Normalized Cohesion and Associated Crest Retreat for an Initially Vertical Slope With $\phi = 50°$

Failure	$c/\gamma H$	CR/H
1	0.094114	0.31201
2	0.035181	0.47837
3	0.018911	0.58549
4	0.01138	0.64988
5	0.006817	0.68838
6	0.004074	0.7114
7[a]	0.003084	0.75056

[a]The seventh mechanism is relative to the black line in Figure 8a.

mechanisms, a deep seated mechanism involving the whole slope profile, from the toe up to the crest, could occur for the case of $\lambda > \phi$ (see Figure 8). To calculate this deep mechanism, the following steps have been taken.

[29] 1. The linear envelope to the piecewise log spiral profile obtained for $c^m \sim 0$ (see Figure 8) is drawn. The height of this new linear profile (0.9H in case of $\phi = 50°$) is lower than the original slope height, H, since its lowest point is located at the point where the envelope touches the first log spiral failure line (point A in Figure 8).

[30] 2. The envelope line is assumed as the new slope profile. Since its inclination λ is larger than ϕ, there must exist a value of cohesion $c^{1*} > c^m$ for which a failure occurs (herein named failure 1*). This value has been determined

by applying equation (3) to determine the critical c value and failure surface for a planar slope profile.

[31] 3. The value of cohesion c^{1*} associated with the occurrence of this mechanism is compared with the cohesion values $c^1, c^2, \ldots c^m$ of the series of log spiral mechanisms previously determined. The exact sequence of failures will be given by $c^1, c^2, \ldots c^i, c^{1*}$ with $c^{1*} > c^{i+1}$.

[32] 4. When the cohesion becomes lower than c^{1*}, the slope profile is made by the single log spiral failure surface associated with the mechanism determined in step 3. Subsequent failures will depart from this profile. To look for the next failure, equation (4) and the procedure described in section 3.2.2 must be applied. The new failure is characterized by a cohesion value $c^{2*} < c^{1*}$ (see dashed line in Figure 8).

[33] 5. Subsequent failures may be found by applying the procedure described in section 3.2.3 until the cohesion becomes negligible, $c^{m*} \sim 0$. Then, a new linear envelope to the obtained piecewise log spiral slope profile may be drawn. If the inclination λ^* of the envelope is close to the friction angle, the procedure is stopped, otherwise all the listed steps are repeated again, starting from step 1 as many times as required.

[34] Note that in step 3 an approximation has been introduced. In fact, in the calculation of the deep log spiral failure mechanism (occurring at $c = c^{1*}$) the slope profile is

Table 2. Values of Normalized Cohesion and Associated Crest Retreat for Slopes With Initial Inclination β, Crest Inclination α, and Friction Angle ϕ

	$\beta = 90$						$\beta = 80$						$\beta = 70$					
	$\phi = 40$		$\phi = 30$		$\phi = 20$		$\phi = 40$		$\phi = 30$		$\phi = 20$		$\phi = 40$		$\phi = 30$		$\phi = 20$	
Failure	$c/\gamma H$	CR/H	$c/\gamma H$	CR/H	$c/\gamma H$	CR/H	$c/\gamma H$	CR/H	$c/\gamma H$	CR/H	$c/\gamma H$	CR/H	$c/\gamma H$	CR/H	$c/\gamma H$	CR/H	$c/\gamma H$	CR/H
								$\alpha = 5$										
1	0.121	0.415	0.151	0.524	0.183	0.651	0.0866	0.3131	0.116	0.427	0.150	0.563	0.05858	0.225	0.0877	0.339	0.122	0.484
2	0.0502	0.666	0.0680	0.868	0.0927	1.138	0.0392	0.5493	0.0569	0.766	0.0821	1.056	0.0307	0.410	0.0476	0.635	0.0724	0.962
3	0.0295	0.842	0.0439	1.140	0.0678	1.580	0.0265	0.7078	0.0412	1.021	0.0660	1.486	0.0206	0.533	0.0353	0.853	0.0624	1.369
4	0.0195	0.959	0.0322	1.338	0.0572	1.952	0.0175	0.8120	0.0301	1.206	0.0555	1.847	0.0137	0.615	0.0258	1.012	0.0524	1.709
5	0.0128	1.035	0.0234	1.482	0.0478	2.263	0.0115	0.8807	0.0219	1.341	0.0463	2.148	0.00899	0.668	0.0188	1.128	0.0438	1.994
6	0.00842	1.085	0.0170	1.586	0.0399	2.523	0.00757	0.9257	0.0160	1.440	0.0387	2.400	0.0059	0.704	0.0137	1.212	0.0366	2.232
7	0.00553	1.118	0.01235	1.662	0.0333	2.740	0.00497	0.9554	0.01160	1.511	0.0323	2.610	0.00387	0.727	0.00993	1.272	0.0305	2.431
8	0.00363	1.140	0.00897	1.717	0.0278	2.921	0.00327	0.9749	0.00842	1.563	0.0270	2.786	0.00254	0.742	0.00721	1.317	0.0255	2.596
9	0.00238	1.154	0.00652	1.757	0.0232	3.072	0.00215	0.9877	0.00612	1.600	0.0225	2.932	0.00167	0.752	0.00524	1.349	0.0213	2.735
10	0.00156	1.164	0.00473	1.786	0.0194	3.198	0.00141	0.9961	0.00444	1.627	0.0188	3.055	0.00109	0.759	0.0038	1.372	0.0178	2.850
								$\alpha = 0$										
1	0.121	0.403	0.150	0.504	0.182	0.618	0.0861	0.302	0.115	0.407	0.148	0.529	0.0583	0.214	0.0871	0.320	0.120	0.449
2	0.0478	0.629	0.0641	0.807	0.0863	1.031	0.0376	0.518	0.0540	0.707	0.0767	0.949	0.0296	0.384	0.0452	0.585	0.0677	0.860
3	0.0274	0.785	0.0399	1.038	0.0601	1.392	0.0248	0.660	0.0378	0.926	0.0589	1.302	0.0195	0.496	0.0326	0.774	0.0559	1.195
4	0.0177	0.886	0.0283	1.202	0.0484	1.680	0.0160	0.751	0.0267	1.081	0.0471	1.583	0.0125	0.567	0.0230	0.907	0.0447	1.461
5	0.0113	0.950	0.0199	1.317	0.0385	1.910	0.0103	0.810	0.0188	1.189	0.0375	1.806	0.00804	0.613	0.0162	1.001	0.0356	1.674
6	0.00725	0.991	0.0139	1.398	0.0306	2.092	0.00658	0.847	0.0131	1.265	0.0298	1.984	0.00515	0.642	0.0113	1.067	0.0282	1.842
7	0.00464	1.018	0.00977	1.454	0.0243	2.237	0.00421	0.871	0.00922	1.319	0.0236	2.125	0.00329	0.661	0.00796	1.113	0.0224	1.976
8	0.00297	1.035	0.00685	1.494	0.0193	2.352	0.00270	0.887	0.00646	1.356	0.0188	2.237	0.00211	0.673	0.00558	1.145	0.0178	2.082
9	0.00190	1.046	0.00480	1.522	0.0153	2.443	0.00172	0.897	0.00453	1.382	0.0149	2.326	0.00135	0.681	0.00391	1.167	0.0141	2.166
10	0.00122	1.053	0.00337	1.541	0.0122	2.516	0.00110	0.903	0.00318	1.401	0.0118	2.396	0.00086	0.686	0.00274	1.183	0.0112	2.233
								$\alpha = -5$										
1	0.120	0.395	0.149	0.489	0.180	0.594	0.0857	0.293	0.114	0.391	0.147	0.503	0.05806	0.206	0.0865	0.306	0.119	0.423
2	0.0457	0.600	0.0607	0.760	0.0807	0.952	0.0361	0.49338	0.0514	0.662	0.0721	0.870	0.0286	0.365	0.0432	0.547	0.0639	0.784
3	0.0255	0.740	0.0364	0.961	0.0537	1.253	0.0234	0.622	0.0349	0.855	0.0531	1.167	0.0185	0.467	0.0303	0.714	0.0508	1.068
4	0.0161	0.829	0.0251	1.099	0.0416	1.485	0.0148	0.704	0.0240	0.987	0.0408	1.395	0.0116	0.530	0.0207	0.828	0.0389	1.285
5	0.0101	0.884	0.0171	1.193	0.0317	1.662	0.0093	0.755	0.0163	1.076	0.0311	1.568	0.00726	0.570	0.0141	0.906	0.0296	1.450
6	0.00628	0.919	0.0116	1.257	0.0241	1.797	0.00577	0.786	0.0110	1.137	0.0237	1.700	0.00454	0.595	0.0096	0.959	0.0226	1.576
7	0.00393	0.940	0.00786	1.301	0.0184	1.899	0.00361	0.806	0.00749	1.178	0.0180	1.800	0.00283	0.611	0.00649	0.994	0.0171	1.672
8	0.00245	0.954	0.00533	1.330	0.0140	1.977	0.00225	0.819	0.00508	1.206	0.0136	1.876	0.00177	0.621	0.0044	1.019	0.0130	1.744
9	0.00153	0.962	0.00362	1.350	0.0106	2.036	0.00141	0.827	0.00345	1.225	0.0104	1.934	0.0011	0.627	0.00299	1.035	0.0099	1.799
10	0.00096	0.968	0.00246	1.364	0.0081	2.081	0.00088	0.831	0.00234	1.238	0.0079	1.978	0.00069	0.630	0.00203	1.046	0.0075	1.842

Table 3. Values of Normalized Cohesion and Friction Angle at Failure for an Initially Vertical Slope for the Two Degradation Paths Shown in inset of Figure 13[a]

	Any c^{ini}		$c^{ini} = 0.136$	
Failure	$c/\gamma H$	ϕ (deg)	$c/\gamma H$	ϕ (deg)
1	0.1572	27.50	0.1270	34.91
2	0.0690	27.50	0.0739	28.67
3	0.0440	27.50	0.0503	26.04
4	0.0321	27.50	0.0397	24.81
5	0.0232	27.50	0.0312	23.81
6	0.0167	27.50	0.0245	23.01
7	0.0120	27.50	0.0193	22.38
8	0.0087	27.50	0.0152	21.89
9	0.0063	27.50	0.0120	21.49
10	0.0045	27.50	0.0095	21.18
11	0.0032	27.50	0.0075	20.94
12	0.0023	27.50	0.0059	20.75
13	0.0017	27.50	0.0047	20.59
14	0.0012	27.50	0.0037	20.47
15	0.0009	27.50	0.0029	20.38
16	0.0006	27.50	0.0023	20.30
17	0.0005	27.50	0.0018	20.24
18	0.0003	27.50	0.0015	20.19
19	0.0002	27.50	0.0012	20.16
20	0.0002	27.50	0.0009	20.13

[a]In the "any c^{ini}" category, constant friction $\phi^{ini} = 27.5$, whereas in the "$c^{ini} = 0.136$" category $\phi^{ini} = 35$ and $\phi^{fin} = 20$.

assumed to be planar (the linear envelope constructed in step 1), but the calculated log spiral failures from $i+1$ to m do not take place in reality. Therefore the slope profile from which the 1* failure has been calculated is not entirely a plane: it should be approximated by a plane in its lower part and a log spiral in its upper part (see the region enclosed by the solid oval in Figure 8). But since the region delimited by the log spiral is small in comparison with the rest of the profile, the influence of this approximation on the calculation of the successive mechanisms can be neglected. Moreover, it was found that for $\phi < 40°$, the linear envelope obtained at $c^m \sim 0$ has an inclination λ very close to ϕ, therefore it was not necessary to perform steps 2–5. In the example considered here, $\phi = 50°$, the calculation was stopped at the eighth mechanism, represented by a dash-dotted line in Figure 8 (see results in Table 1).

[35] In Table 2, some results obtained by implementing the described procedure in Matlab are shown. The values of cohesion normalized by the initial slope height and unit weight, $c/\gamma H$, and crest retreat normalized by the initial height, CR/H, are listed for different ϕ values; initial slope inclinations, β; and crest inclinations, α. Figure 9 shows the relationship obtained between cohesion and crest retreat. From these results it emerges that the average inclination of the final slope profile is strongly dependent on the assumption of constant ϕ, as it will be shown in section 3.5 where this hypothesis has been removed.

3.4. The Evolution of the Warden Point Cliff

3.4.1. Introduction

[36] In general, it is difficult to find accurate data relating to the mode and times of evolution of a slope subjected to successive and/or retrogressive failures. The chosen case study concerns the evolution of a steep scarp at Warden Point, Isle of Sheppey (Kent, England) [*Hutchinson*, 2001] where a deep-seated rotational slide occurred on 21

November 1971. This slide, in a 43 m high cliff, by the sea, occurred in the London Clay formation, and left a steep rear scarp about 15 m high, the degradation of which was monitored for 902 days [*Gostelow*, 1974]. Since the lower part of the slope is almost unaffected by weathering because it is protected by the accumulated debris, the limit analysis model has been applied to the upper part of the slope (between points A and B in Figure 10). In this case the hypothesis of complete removal of the debris after each failure mechanism is fully verified.

3.4.2. Crest Retreat-Weathering Relation

[37] Since the material friction angle is unknown, a back analysis procedure is needed to determine it. In this case the final crest retreat, $CR_{fin}/H = 0.71$, is inferred from the observed final profile (see Figure 10). The inclination of the initial profile ($\beta = 60.6°$) was also inferred from Figure 10. We assume that only the cohesion decreases because of weathering. Our model was run for various values of ϕ until satisfactory agreement of the final slope profile (at $c = 0$) was achieved with the observed one. A friction angle of $\phi = 24.5°$ was obtained. A 5th degree polynomial function (see Figure 11) was used to interpolate the values of cohesion at failure obtained by the model. The initial value of cohesion (c at t = 0) was taken as the y intercept of the polynomial interpolating function in Figure 11.

#### 3.4.3. Time-Weathering Relation

[38] The experimental data show the evolution of the cliff in terms of crest retreat versus time so it is necessary to introduce a time scale in the limit analysis model. To this end, four weathering laws (linear, parabolic, hyperbolic, and exponential), all depending on two parameters, between time and cohesion decrease have been introduced:

$$\begin{aligned} c &= K_1 t + K_2, \\ c &= \frac{K_1}{t + K_2}, \\ c &= K_1 \left(1 - \frac{t}{K_2}\right)^2, \\ c &= K_1 \exp\left(-\frac{t}{K_2}\right). \end{aligned} \quad (6)$$

In order to obtain crest retreat-time relationships, the time-cohesion relationships of equation (6) were substituted into the cohesion-crest retreat relationship achieved by the limit analysis model for $\phi = 24.5°$. One of the two parameters in equation (6) was determined by imposing the initial condition of no retreat ($CR = 0$ at t = 0), while the other was varied until the best fit of the crest retreat-time experimental data was obtained.

[39] Figure 12 shows the crest retreat-time curves obtained by substituting the selected time-cohesion relationships (equation (5)) into the cohesion-crest retreat relationship achieved by limit analysis. The hyperbolic law is the one which makes the calculated solution fitting the experimental curve satisfactorily.

[40] From a comparison of the failure lines (Figure 12b), very good agreement between observed and predicted slope profiles can be noted. The evolution of the monitored cliff is characterized by a series of concave profiles taken at specific times, and not just after the occurrence of a particular slope failure. A similar pattern was observed over
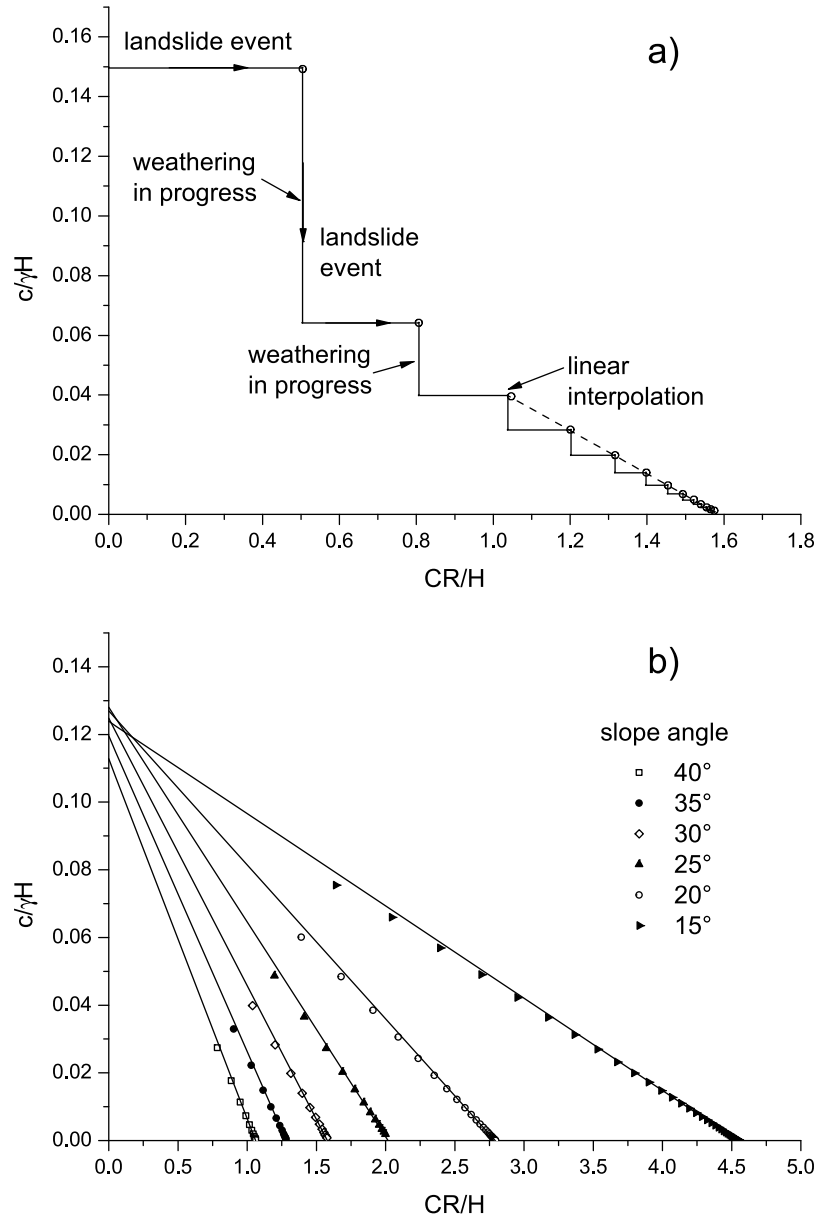
Figure 9. Dimensionless normalized cohesion versus crest retreat ($\beta = 90°$). (a) Step-like relationship between cohesion and crest retreat obtained for $\phi = 30°$; circles represent values obtained by limit analysis. (b) If the first two failures are excluded, the values of critical cohesion and crest retreat lie on straight lines.

19 years [*Wallace*, 1980] for the degradation of a 4.5 m high normal fault scarp in morainic material in Montana.

3.5. Cohesion and Friction Decrease

[41] In this section, the limit analysis model is presented to include the case of both cohesion and friction decreasing over time. This hypothesis is visualized in the $c/\gamma H$-ϕ plane (Figure 6a) by an inclined straight line. The internal friction angle decreases from an initial value, ϕ^{ini}, to a final one, ϕ^{fin} (Figure 1d) and the cohesion decreases from an initial value, c^{ini}, to zero. Depending on ϕ^{ini}, ϕ^{fin} and the initial cohesion assumed, different kinds of slope evolution take place. These three independent parameters (ϕ^{ini}, ϕ^{fin}, c^{ini}) are graphically represented by the location of point $P(c^{\text{ini}}, \phi^{\text{ini}})$

and the inclination of the straight line in the $c/\gamma H$-ϕ plane (see Figure 6a). In Figure 6b, the algorithm implemented to determine the critical c, ϕ values for each failure is illustrated. Unlike the case of cohesion reduction at constant ϕ, an initial value of cohesion now needs to be specified at the beginning of the analysis. In fact, given ϕ^{ini} and ϕ^{fin}, different values of c^{ini} would imply different inclinations of the straight lines in Figure 6a, and therefore different weathering paths. On the contrary, in the case of constant ϕ, the path in the $c/\gamma H$-ϕ plane is along a vertical line, independent of the value of c^{ini}.

[42] A couple of examples are proposed in this section in order to illustrate the influence of the various parameters on the slope evolution. In any case it is important to verify if a
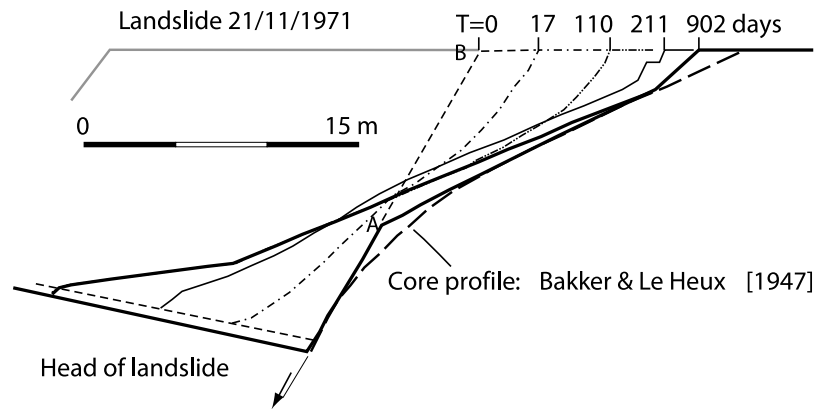
Figure 10. Observed profiles of the monitored rear scarp at Warden Point in a London Clay formation during 902 days of degradation [after *Hutchinson*, 2001].

simplified analysis, using a time averaged (i.e., constant) ϕ, produces results accurate enough so that the variation of ϕ over time can be modeled in a simpler way. In Figure 13, the case of an initially vertical cliff characterized by $\phi^{ini} = 35°$ and $\phi^{fin} = 20°$ is compared with that of a cliff subject to cohesion decrease only and characterized by a constant friction angle ϕ taken as: $\phi^{ave} = (\phi^{ini} + \phi^{fin})/2$. In the inset of Figure 13, the two degradation paths are shown in the $c/\gamma H$-ϕ plane. As discussed in the previous paragraph, the results obtained in the case of ϕ varying over time depend on the initial cohesion as well, that is, different initial values of cohesion are associated with lines in the $c/\gamma H$-ϕ plane with different inclinations and therefore leading, in principle, to different results in terms of slope evolution. Among the infinite possible values of initial cohesion it was decided to consider the value for which the initially vertical slope is about to experience its first failure. This value has been

determined with an iterative procedure. This choice implies that the degradation path chosen is the one where the variation of ϕ matters the most in terms of soil strength, so it is the right case to evaluate the maximum influence that the variation of ϕ might have on the slope evolution. Looking at Figure 14a, the higher the initial cohesion, the steeper the straight line in the $c/\gamma H$-ϕ plane becomes. As is shown in Figure 14b, higher values of initial cohesion imply that the series of failures occur for lower values of ϕ (i.e., values of ϕ closer to ϕ^{fin}) and therefore the influence of the variation of ϕ becomes smaller.

[43] It can be observed (Figure 13) that a cliff subject to ϕ decreasing over time undergoes a final crest retreat significantly larger than a cliff characterized by a constant average friction angle. This observation leads to the conclusion that the variation of ϕ cannot be neglected without introducing a significant error. The difference amounts to
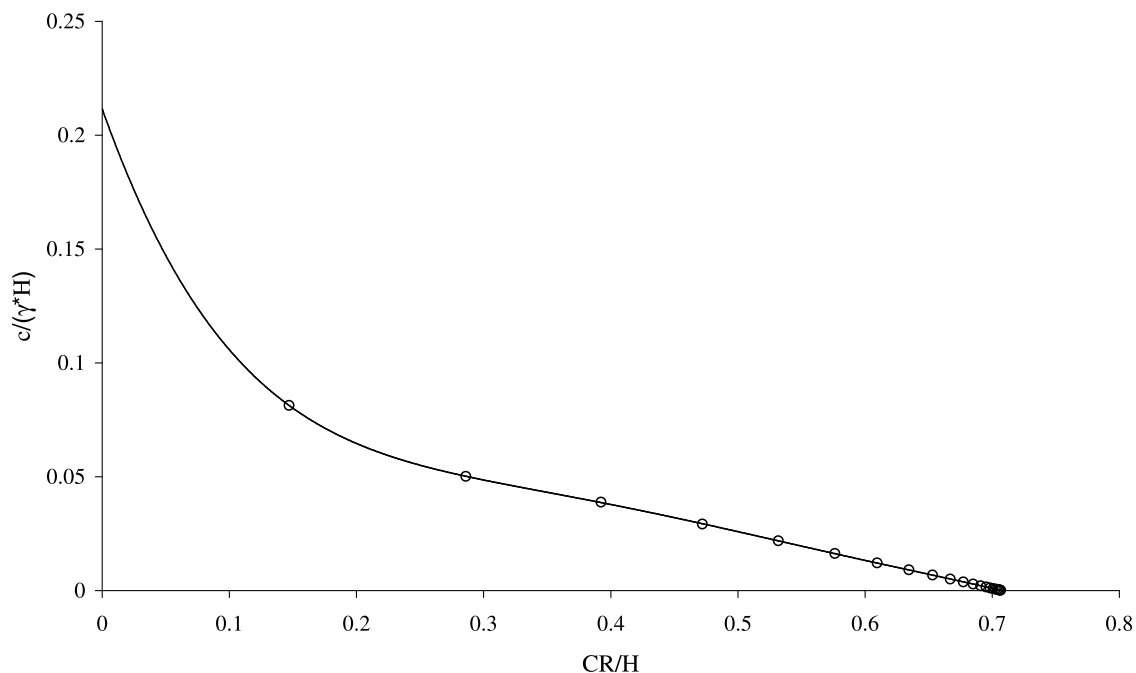
Figure 11. Normalized cohesion versus crest retreat predicted by the model: the values (circles) obtained by limit analysis have been interpolated by a 5th polynomial degree.
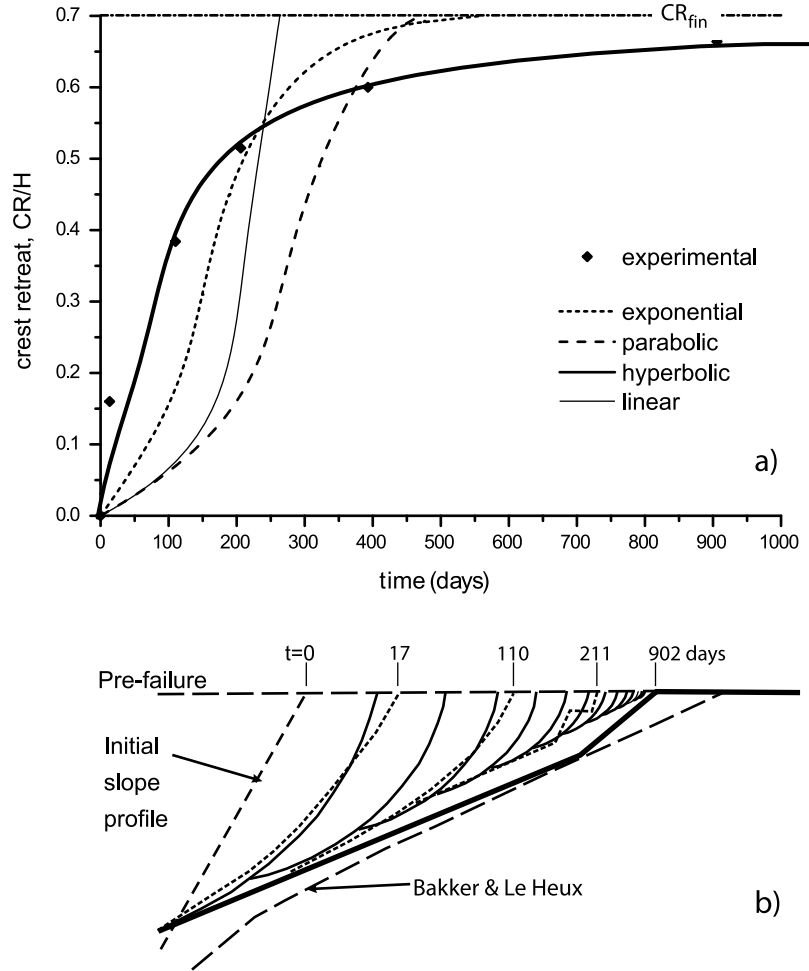
Figure 12. Evolution of the Warden Point cliff: comparison between experimental data [after *Hutchinson*, 2001] and model predictions for different laws of weathering over time. (a) Comparison of the obtained crest retreat-time relationships. (b) Comparison in terms of failure mechanisms.

23%, demonstrating that for any degradation scenario involving a significant variation of ϕ, this variation has to be modeled explicitly. Finally, looking at the final profiles, the case of ϕ varying over time gives rise to a rather convex shape instead of the linear one typical for the case of constant ϕ (see Figure 13).

[44] Figure 14 shows a comparison between cliffs subject to the same decrease of friction angle, but with different initial values of cohesion. This analysis is useful to understand the role played by the initial cohesion on cliff evolution. Three cases have been considered: a very high value of initial cohesion ($c^{ini} = 3.0 \times \gamma H$), which for a slope with H = 50 m and γ = 20 kN/m^3 would mean c^{ini} = 3000 kPa, a medium value ($c^{ini} = 0.3 \times \gamma H$) and the lowest possible value $c^{ini} = 0.136 \times \gamma H$. This last value has been determined by iteration as the value for which a vertical cliff is at impending failure. In Table 4, the values of c, ϕ for each successive failure are reported. The case of very high initial cohesion gives rise to the longest crest retreats. This can be explained by looking at the values of ϕ for each failure (Table 4); these are the lowest values in comparison with the two other cases analyzed. This is in agreement with the observations of section 3.2, where it emerged that the lower the friction angle, the larger the crest retreat. The case of

minimum initial cohesion is associated with the smallest crest retreats. So a clear trend emerges with higher c^{ini} associated with larger crest retreats.

[45] Let us now consider envelopes to the final profiles. In the case of very high initial cohesion, the envelope is a straight line as in the case of constant ϕ (see section 3.2). In fact, in this case, the values of ϕ at failure are almost constant and close to 20°. Since the final inclination λ is lower than ϕ^{fin}, no more failures are expected and the achieved profile is the final one. Instead, in case of an intermediate value for the initial cohesion, the envelope is bilinear. Since the inclination of the steeper part of the bilinear envelope is greater than the final friction angle, this cannot be the final profile and further global mechanisms, as shown in Figure 8, can be expected. Unlike the case in Figure 8, here the profile in step 2 (see section 3.2) is made up of two linear segments with different inclinations rather than one, therefore the analytical formulation becomes more complex, even though it is still feasible (see the case $\alpha \neq 0$ in Appendix A). In the third case, $c^{ini} = 0.136 \times \gamma H$, the final envelope is composed of four linear segments. The steepest part of the envelope is higher than the final friction angle; therefore, further mechanisms starting from the toe of the slope have to be expected. In this case,
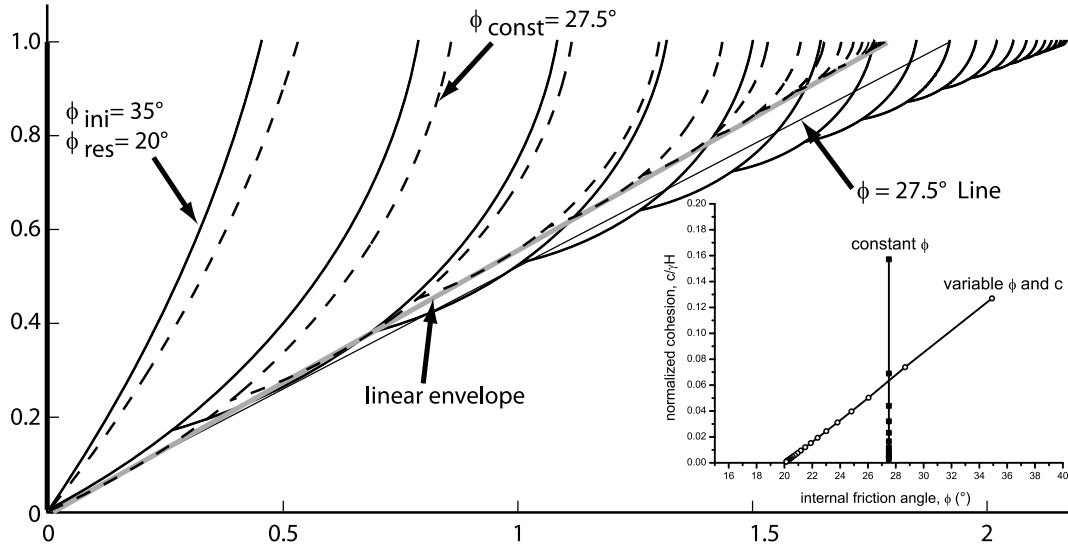
Figure 13. Slope evolution for an initially vertical cliff for two degradation paths: constant and variable ϕ. Inset is a representation of the degradation paths in the $c/\gamma H$-ϕ plane (the dots represent the values of c, ϕ at failure as reported in Table 3). The vertical path is for the case of constant friction ($\phi^{const} = 27.5$); the inclined path is for the case of variable friction ($\phi^{ini} = 35$, $\phi^{fin} = 20$, $c^{ini} = 0.136 \times \gamma H$). The thin straight line represents the inclination of $\phi = 27.5$.

unfortunately, the model is unable to predict the evolution since an analytical formulation for a slope profile made up of more than two straight lines becomes prohibitive.

3.6. Transport Law

[46] *Dietrich et al.* [2003] define a geomorphic transport law as a mathematical expression, derived from a physical mechanism, of mass flux or erosion caused by processes acting over geomorphically significant spatial and temporal scales. To evaluate the mass flux over time, the volume of the failing blocks must be computed. Considering a unit slope width, the transported volume can be easily derived from the areas of the detached material. By plotting the cumulative frequency values for the area of the detached blocks on a semilogarithmic plot, a linear relationship is found (see Figure 15). This relationship fits the evolution of the computed retrogressive phenomena except for the earliest failures. In fact, this relationship is valid for all the failures after the first and/or the second. In general, the deviation from the logarithmic relationship is minimal for high friction angles and becomes progressively more significant for smaller friction angles, involving progressively both the first and second failures. This type of relationship is the result of the initial inclination of the slope, the fact that the failing blocks after the first to third failure present the same shape, and the relative role played by friction and cohesion in terms of the shear strength of the material (i.e., the cohesive contribution to the material strength decreases after each landslide).

[47] Figure 16a shows the relationship between the size of the slope failures, in terms of normalized area (A/H^2), with respect to the normalized cohesion, which is also the reciprocal of the stability number, for ϕ values ranging from 15° to 40°. The plot shows that larger failures occur for large values of $c/\gamma H$ which occur at the beginning of the slope weathering process (when c has still high values),

after which progressively smaller volumes of material are involved in the mass flux. This is true with the exception of the first failure, since the detaching area can be smaller than the one relative to the second failure, as in the case of $\beta = 70°$. If the first failure is disregarded, the points in the plot are well fitted by the following power relationship:

$$c/\gamma H = k_1 \sqrt{A/H^2}, \tag{7}$$

where the constant k_1 varies with ϕ. Therefore the square root of the normalized area is proportional to the normalized cohesion.

[48] The transport law can now be investigated by looking at the relationship between the mass of the failing blocks which is proportional to their cross-sectional area, and the average gradient of the evolving slope. The average gradient is found by integrating the slope gradient along the entire profile:

$$s_{ave} = \frac{\int_0^L f'(X)dX}{L} = \frac{f(L) - f(0)}{L} = \frac{H}{L}, \tag{8}$$

where X is the abscissa coordinate, L the horizontal distance between the slope crest and toe, and $f = f(X)$ is the function expressing the slope profile in Cartesian coordinates with the origin taken at the slope toe. In Figure 16b the relationship between mass flux (in terms of normalized detached area) and average slope gradient is shown. Disregarding the first failure, the data may be well fitted by either third degree polynomials or allometric laws (see Figure 16). It is important to note that the areas considered here are cross-sectional areas relative to the evolution of a single slope by a sequence of retrogressive failures, rather than areas of landslides developing independently on different slopes, as in the case of an evolving catchment. These areas give an indication of the amount of mass transport over time along a specific slope profile.
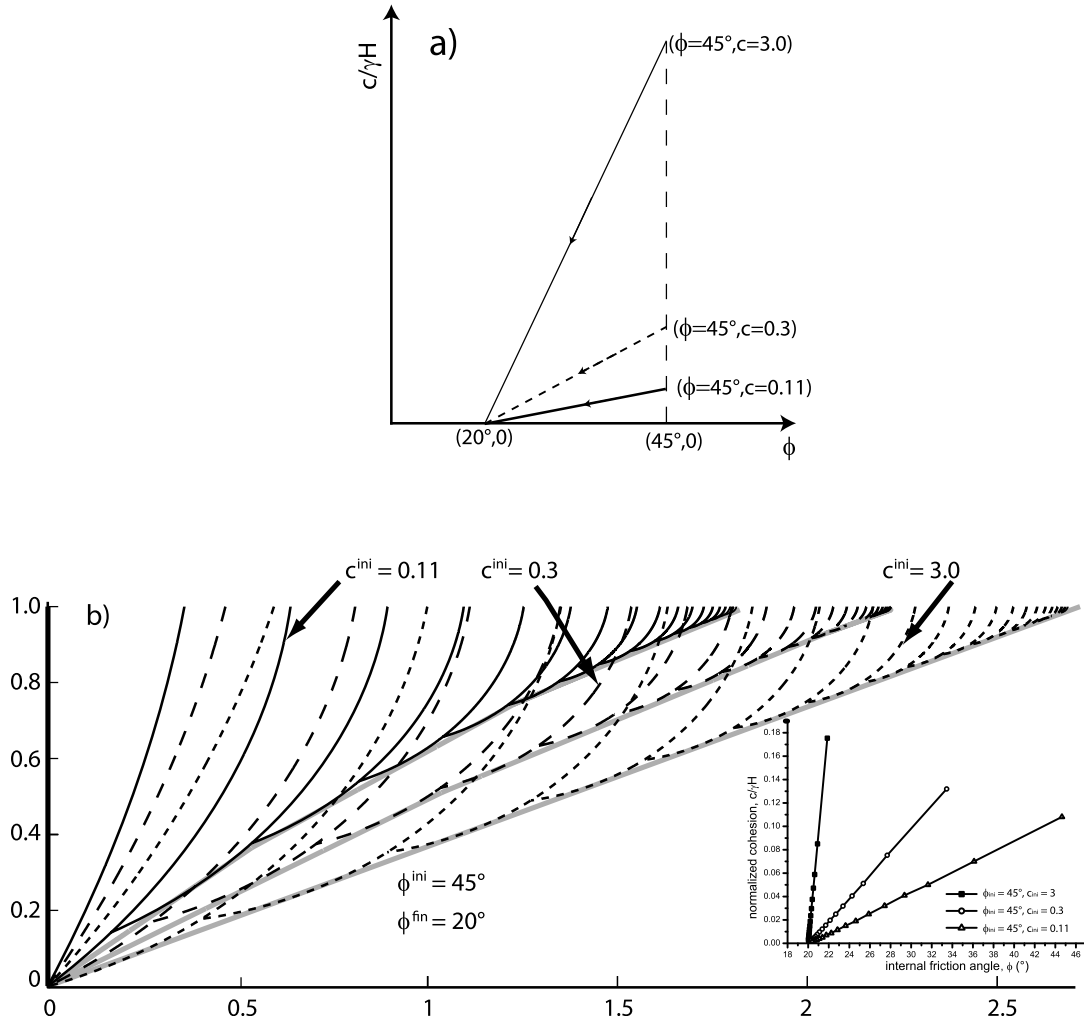
Figure 14. Slope evolution for an initially vertical cliff for three different degradation paths all having $\phi^{ini} = 45$, $\phi^{fin} = 20$ but different values of initial cohesion: $c^{ini} = 0.11 \times \gamma H$, $c^{ini} = 0.3 \times \gamma H$, and $c^{ini} = 3.0 \times \gamma H$. (a) Graphical representation of the degradation paths in the $c/\gamma H$-ϕ plane. (b) Profiles obtained for the three degradation paths considered; the gray straight lines underneath the log spirals represent the linear envelopes. In the inset, the dots along the lines represent the ϕ, c values, reported in Table 4, at which failures take place.

[49] The results are independent of time. In order to investigate the time of evolution of retrogressive slopes it is necessary to make an assumption in terms of the weathering/alteration law. This information is very difficult to determine since it would require the investigation of the complex physical and chemical alteration processes taking place within the slope [e.g., *Heimsath et al.*, 1997; *Anderson et al.*, 2002; *Marques et al.*, 2010; *White and Brantley*, 2003; *White et al.*, 2008, 2009]. Here we investigate simple alteration laws, beyond those in equation (6) expressed in terms of time-cohesion decrease, $c = c(t)$, and characterized by two parameters only (see Figure 17):

$$c = K_1(1 - K_2 t^n),$$
$$c = K_1(1 - K_2 \ln(1 + t)), \qquad (9)$$
$$c = \sqrt{K_1 t + K_2}.$$

The choice of the initial point in the c − time chart is clearly arbitrary. It was decided to take the initial time as immedi-

ately after the first failure, therefore $c^{ini} = c(t = 0) = c^1$ where c^1 is the value of c when the first failure occurs. This choice is due to the fact that the initial conditions of natural slopes are in general unknown, apart from rare cases such as the one described in section 3.4, where the time of formation of the initial slope is given by the occurrence of a landslide event. Moreover the first failure needs to be discarded if we want to use equation (7) to relate cohesion to mass flux. The same final condition expressed in terms of a dimensionless time ($t_{fin} = 1$) has been assumed for all the $c = c(t)$ relationships for consistency. Note that from a physical point of view, the condition of zero cohesion might never be reached; in this case the final time would be given by the time the cohesion has reached its ultimate residual value. The parameters of all the relationships have been calibrated to satisfy both the initial and final conditions. It is realistic to expect that the decrease of soil strength is high at first, after which more and more time is needed to develop full degradation since particle/grain/crystal debonding can occur more rapidly than

Table 4. Values of Normalized Cohesion and Friction Angle at Failure for an Initially Vertical Slope for Different Initial Values of Cohesion[a]

|	$c^{ini} = 3.0$		$c^{ini} = 0.3$		$c^{ini} = 0.11$	
Failure	$c/\gamma H$	ϕ (deg)	$c/\gamma H$	ϕ (deg)	$c/\gamma H$	ϕ (deg)
1	0.1754	21.86	0.1393	33.45	0.1081	44.64
2	0.0850	20.91	0.0753	27.68	0.0637	36.11
3	0.0588	20.63	0.0512	25.35	0.0439	31.63
4	0.0472	20.51	0.0405	24.26	0.0345	29.35
5	0.0375	20.40	0.0318	23.38	0.0271	27.42
6	0.0297	20.32	0.0250	22.68	0.0212	25.88
7	0.0236	20.25	0.0197	22.13	0.0166	24.62
8	0.0187	20.20	0.0155	21.70	0.0130	23.63
9	0.0148	20.16	0.0122	21.36	0.0103	22.85
10	0.0118	20.12	0.0097	21.09	0.0081	22.24
11	0.0093	20.10	0.0076	20.87	0.0064	21.76
12	0.0074	20.08	0.0060	20.70	0.0050	21.38
13	0.0059	20.06	0.0048	20.57	0.0040	21.08
14	0.0047	20.05	0.0038	20.46	0.0031	20.84
15	0.0037	20.04	0.0030	20.38	0.0025	20.65
16	0.0029	20.03	0.0024	20.31	0.0020	20.50
17	0.0023	20.02	0.0019	20.26	0.0016	20.38
18	0.0019	20.02	0.0015	20.21	0.0012	20.28
19	0.0015	20.01	0.0012	20.18	0.0010	20.21
20	0.0012	20.01	0.0009	20.15	0.0008	20.15

[a]Case shown in Figure 14.

chemical/mineralogical transformation. Most of the considered $c = c(t)$ relationships respect this physical principle with the exception of the square root law ($c = \sqrt{k_1 t + k_2}$). This last relationship gives rise to a transport rate which is constant on average.

[50] The decrease of the detached areas with time, according to different weathering laws, is shown in Figure 18a. The area of the unstable slices and the associated times of failure, which are linked to the weathering rate, allow for the estimation of a rate of mass production and transport from the slope failures. The transport law for the case of the slope evolution by retrogressive landsliding, under weathering-limited conditions, can be examined by analyzing the relationship between the cross-sectional area of the failing blocks and the average slope gradient. In Figure 18b, transport rates for different weathering laws averaged over the time intervals between successive landslide events are plotted.

[51] At this point we might wonder if the transport law achieved might be related somehow to a diffusion model [e.g., *Kirkby*, 1987, *Scheidegger*, 1961; *Kirkby*, 1971; *Carson and Kirkby*, 1972; *Nash*, 1980a; *Pierce and Colman*, 1986; *Andrews and Bucknam*, 1987; *Fernandes and Dietrich*, 1997; *Roering et al.*, 1999; *Martin and Church*, 1997, 2004; *Pelletier et al.*, 2006] and if it might be possible to define an equivalent coefficient of diffusivity for the mass transported along the slope by the sequence of landslides taking place. The shape, gradient and curvature of the profiles achieved by the linear or nonlinear diffusion (e.g., cubic, linear plus cubic, sliding) equations are completely different from the ones generated through our model of the slope evolution. This result suggests that the evolution of slopes experiencing large landslides under weathering limited conditions cannot be satisfactorily modeled by diffusion, advection nor reaction laws. On the other hand, unlike the diffusion models, the evolution of the slope toe (i.e., area of deposition) is not considered in the presented approach.

[52] Finally, it can be noted that all the relationships obtained in this section are affected by the assumption of constant ϕ; if friction also decreases over time, all the derived results will be changed. The transport law obtained would depend on the decrease of the frictional strength component as well. As shown in section 3.5, there is an infinite number of possible degradation paths in the c, ϕ plane, which depend
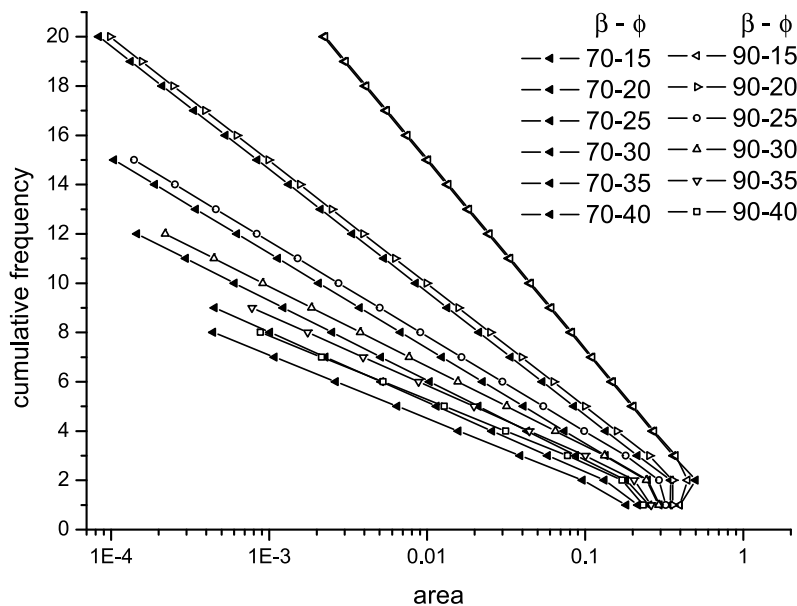
Figure 15. Unstable block area versus cumulative frequency for cliffs with different initial inclinations and internal friction angles. This cumulative frequency represents the number of landslides with area larger than the value on the abscissa. A clear logarithmic relationship exists for failures successive to the first and second ones.
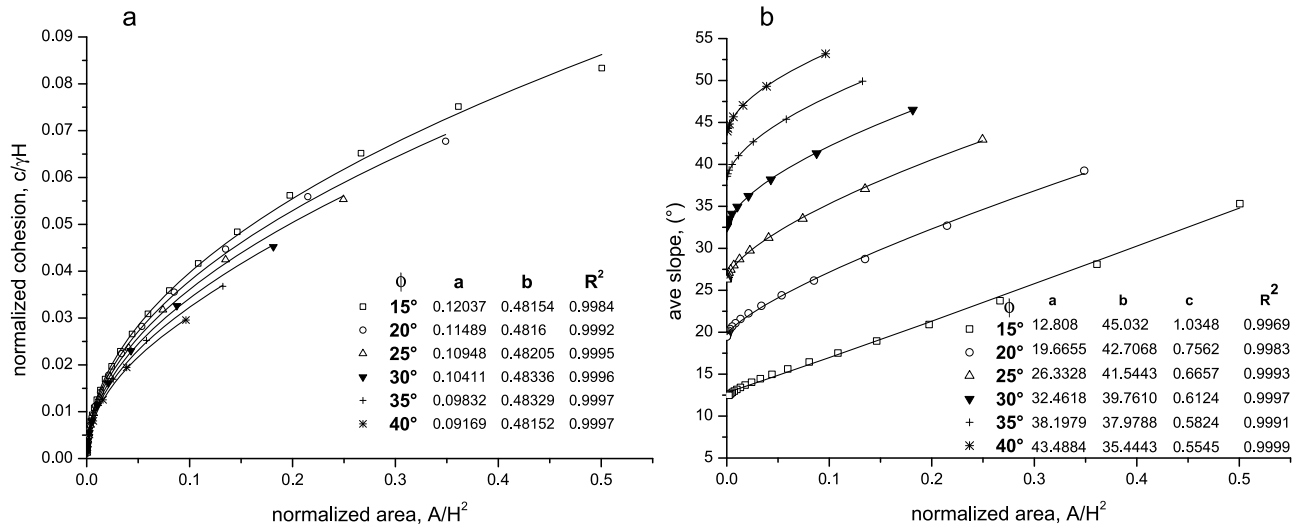
Figure 16. (a) Normalized area of landslide versus normalized cohesion relationship for an initial slope gradient $\beta = 70°$ and variable friction angles ϕ from 15° to 40°. Data are fitted by a power law relationship (square root). (b) Normalized area versus average slope. Data are fitted by allometric laws of the form: $s_{ave} = k_1 + k_2 \times A^{k_3}$.

on the types of weathering processes and geomaterials considered (see Figure 6). Once the alteration laws of c and ϕ have been characterized by means of geotechnical laboratory testing, it becomes possible to obtain the transport law for a particular slope experiencing decrease of both c and ϕ, following the procedure adopted for the case of constant ϕ.

4. Discussion of Results

[53] Hillslope evolution, under weathering limited conditions, has been modeled in this paper by the limit analysis method, associating the evolution of slopes by successive failures along log spiral slip surfaces to the degradation of material strength properties. Degradation has been considered as homogeneous within the entire slope and effects of spatial variability of weathering have been neglected. In general, aggregate models mask the effect of single events of different sizes. This can have little influence over very long time periods, but for shorter time intervals or low weathering rates, it can lead to strong underestimates in the role of single events.

[54] The appeal of the limit analysis approach in comparison with numerical modeling [see *Utili and Crosta*, 2011] is that results are available in an analytical form for the whole range of interest of the mechanical strength parameters (c, ϕ), initial slope inclination (β) and inclination of the slope crest (α). A nomogram showing the evolution of slopes subject to cohesion only decrease is shown (Figure 19) for different values of the aforementioned parameters. In our analyses, slopes are assumed homogeneous, hence the cohesion, friction angle and unit weight values to be used to calculate the stability number, $N = \gamma H/c$, should be taken as the spatial average of the values of the different strata of the slope.

[55] Tables reporting material strength values and crest retreat associated with each successive failure until the attainment of a final stable condition have been presented for various initial inclinations. A simultaneous decrease of both friction and cohesion may also be considered in the

model. This method has been successfully used to model the degradation of a real cliff under continuous basal removal whose evolution over time was available. A very good agreement between measured and predicted profiles is obtained. The evolution is characterized by a series of concave profiles that cannot be predicted with traditional models available in the geomorphologic literature [e.g., *Fisher*, 1866; *Bakker and Le Heux*, 1946; *Kirkby*, 1971] which predict a convex shape for cliffs subject to weathering. These models in fact cannot explicitly take into account the occurrence of a series of discrete mass movements caused by the progressive weakening of material.

[56] In the case of more general conditions (no deposit removal), the method can still be used to obtain a first rough estimation of the expected evolution of the slope, and rejuvenation of the slope profile by erosion of the slope toe
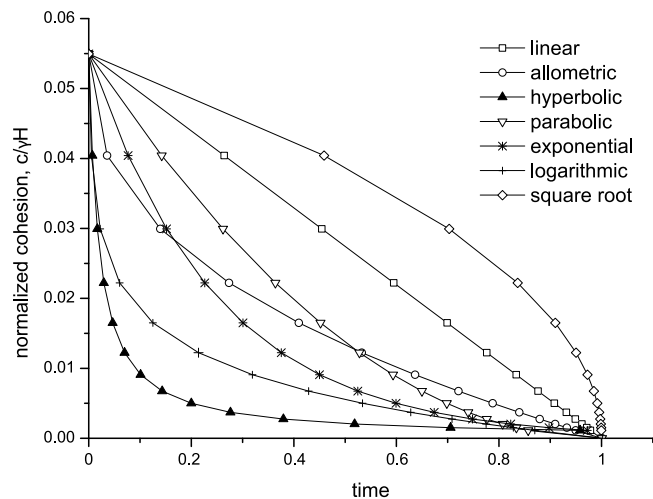
Figure 17. Relationships between normalized cohesion and dimensionless time for the considered weathering laws.
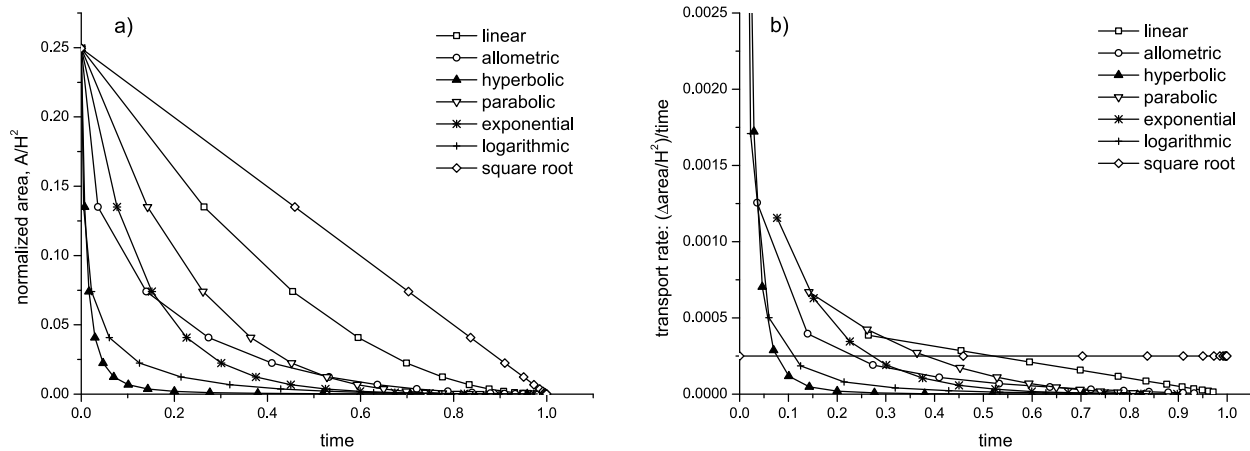
Figure 18. Results obtained according to the different weathering laws assumed. (a) Normalized areas of failing blocks versus dimensionless time; (b) transport rate averaged over discrete time intervals versus dimensionless time.

could be considered and included in the analysis as well. Furthermore, the same approach has general validity for cases characterized by a far-field slope [e.g., *Hanks and Andrews*, 1989]. The effect of a far-field slope on the limit analysis results is shown in Figure 19 and Table 2 for different far-field slope angles ($\alpha = -5°, \alpha = 0°, \alpha = 5°$) and various internal friction angles.

[57] Time dependency can be introduced in the model by means of weathering rate relationships (e.g., linear, power law, exponential), correlating the decrease of material strength with time. As a consequence, slope evolution in time can be simulated and used to forecast crest retreat, and eventually the volume of produced material to be eroded at the slope toe.

[58] The results can be interpreted in terms of a transport law and demonstrate a strong nonlinear relationship between mass flux, time and slope gradient. Nonlinearity is particularly evident when the initial failures (first to the third) are compared with the subsequent ones. This could be the result of

multiple controlling factors. First of all, it must be remembered that all the analyses start with a straight slope. These successively evolve, maintaining log spiral geometry for the slope profile. *Utili and Nova* [2007] demonstrated that if we compare a log spiral slope profile with a planar one, both characterized by the same average slope, $s_{ave} = H/L$, the log spiral one is always more stable than the planar one. Therefore, in case of a log spiral profile, for the same cohesion value, a steeper inclination is required for a failure to occur.

[59] A logarithmic relationship has been found by plotting cumulative frequency values for the area of unstable blocks. Such a relationship seems to govern the evolution of a slope by retrogressive landsliding, which implies dependency between successive failures, except for the very early ones.

[60] In the model, the presence of pore water pressure is not explicitly included, therefore failures are assumed to occur in dry conditions. Clearly this may not be the case in many instances, but it is also possible to include the
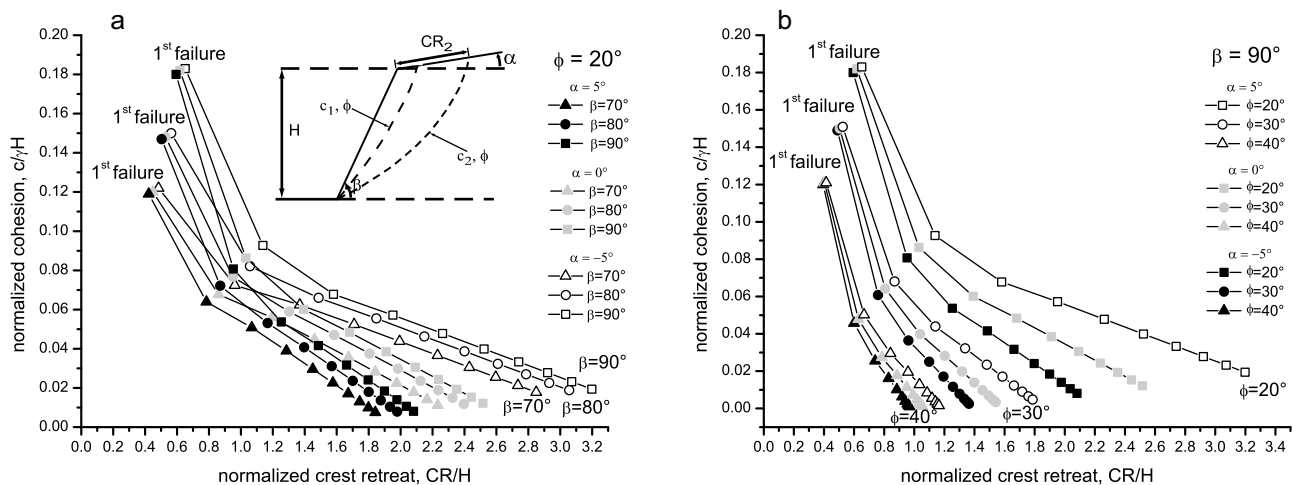
Figure 19. Nomogram of normalized cohesion versus dimensionless crest retreat for constant ϕ cliff evolution. Each point refers to a different failure: (a) for different values of inclination of the upper slope (far-field slope) and initial slope front and (b) for different values of inclination of the upper slope (far-field slope) and various internal friction angles.

presence of water for the simplest cases. To this end, it is necessary to distinguish between two situations: a slope crossed by a phreatic line, made by a layer of dry rock/soil above the phreatic line with or without significant capillary rise (giving rise to a layer of partially saturated soil just above the phreatic line) and fully saturated rock/soil underneath with static hydraulic conditions (no seepage); and a slope subject to steady state (seepage) or transient hydraulic conditions (consolidation) for instance caused by intense rainfall. In the first case, there is no excess water pressure; hence the results obtained by our analyses can still be used running the analyses in terms of effective strengths (c', ϕ'). Under the phreatic line, instead of the total unit weight, γ, the submerged unit weight, γ', would need to be taken. The additional resistance due to capillary effects in the layer of partially saturated soil may be taken into account by increasing the cohesion, adding the effect of the so-called apparent cohesion which is linked to capillary suction according to well established empirical relationships [*Fredlund and Rahardjo*, 1993; *Rao*, 1996]. A spatial average of the values of c' and γ' would need to be taken as input data in the analyses. The second case (seepage or consolidation) is more complex, but if simplifying assumptions about the hydraulic conditions are introduced, the limit analysis upper-bound approach can still be used. However, additional terms in the energy balance need to be introduced and an analytical closed form solution is no longer available [see *Viratjandr and Michalowski*, 2006]. In this case, either a steady state or transient hydraulic analysis is needed. However, these analyses would require the availability of local data such as permeability and hydraulic conditions at the slope boundaries and time varying data such as intensity of rainfall precipitation and evapotranspiration, which are not available over large time spans. Therefore, at present, the complexity of the analyses involved and the lack of experimental data make it an impossible task to take into account the influence of seepage and transient hydraulic conditions into the modeling of slope evolution with the proposed approach.

5. Conclusions

[61] Hillslope evolution under different environmental conditions results in different geometries. In this paper, a model based on geomechanics to predict evolution of slopes has been proposed. With this model it is possible to relate the evolution of natural slopes by a sequence of rotational sliding block failures to the degradation of material strength properties. In the paper, it has been shown how mechanical parameters and their weakening due to weathering affect the slope profiles. The proposed analytical model based on the limit analysis upper-bound method performs well in the determination of slope profiles for weathering-limited conditions, and predicts a strongly nonlinear relationship between mass flux and slope gradient. It can be concluded that with the proposed model it is possible, in principle, to predict the evolution by successive failures of any cliff made either of homogeneous dry rock or cohesive-frictional soils, knowing the strength degradation over time. The proposed model considers strength within the slope to be homogeneous, which is certainly not true. But these uniform c, ϕ values can be thought of as spatial averages of varying c, ϕ

values. To overcome some of these limitations and to have a better understanding of the physical and mechanical processes occurring during slope evolution, it is possible to adopt numerical modeling techniques. This aspect is examined in the companion paper by *Utili and Crosta* [2011] discussing the use of discrete element models to study slope evolution by successive failures, including the effects of deposition of failed material and heterogeneous weathering distribution.

Appendix A

[62] This appendix presents the details of the calculations and mathematical functions used in the limit analysis upper-bound method. We present the calculations for the simpler case of a horizontal cliff crest, $\alpha = 0$ (see Figure 3b). The equations for the more general case of $\alpha \neq 0$ (see Figure A1) are reported in the auxiliary material (see file main_phi_variable_alfa.m).

A1. First Mechanism

[63] Starting with the first mechanism (see Figure 3a), the value of cohesion at failure is given by

$$c = \gamma H \frac{1}{\min_{x,y} f(x,y,\beta,\phi)}, \qquad (A1)$$

where x, y are the angle identifying the log spiral wedge and β is the initial slope inclination;

$$f(x,y,\beta,\phi) = \frac{\{\exp[2\tan\phi(y-x)]-1\}\{\exp[\tan\phi(y-x)]\sin y - \sin x\}}{2\tan\phi(f_1 - f_2 - f_3)} \qquad (A2)$$

with

$$f_1(x,y,\phi) = \frac{\exp[3\tan\phi(y-x)](3\tan\phi\cos y + \sin y) - 3\tan\phi\cos x - \sin x}{3(1 + 9\tan^2\phi)}, \qquad (A3)$$

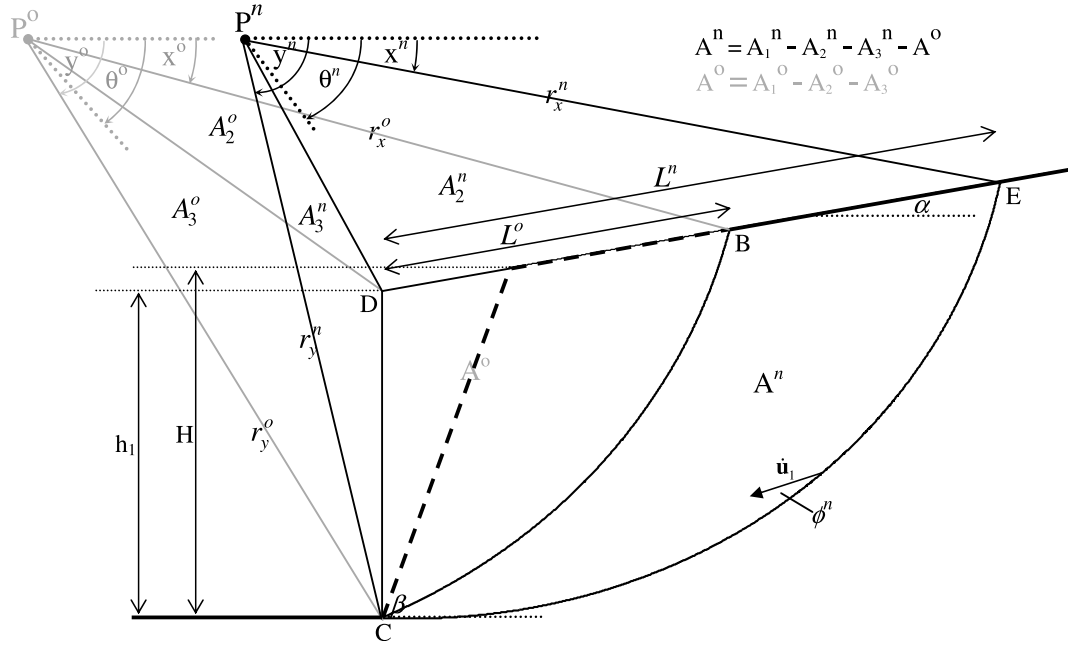$$f_2(x,y,\beta,\phi) = \frac{1}{6}\frac{\sin x}{(\sin\beta)^2}\Big\{-\exp[2\tan\phi(y-x)](\sin(\beta+y))^2 \\ + 2\exp[\tan\phi(y-x)]\cos\beta\sin x\sin(\beta+y) + \\ -(\sin(\beta+x))^2 + 2\sin\beta\cos x\sin(\beta+x)\Big\}, \qquad (A4)$$

and

$$f_3(x,y,\beta,\phi) = \frac{1}{6}\exp[\tan\phi(y-x)]\frac{\sin(\beta+y)}{(\sin\beta)^2} \\ \times\{\exp[2\tan\phi(y-x)]\sin y[\sin(\beta+y)+\sin\beta\cos y] + \\ -2\exp[\tan\phi(y-x)]\sin x\sin(\beta+y) + \\ +\cos\beta(\sin x)^2\}. \qquad (A5)$$

A2. Second and Successive Mechanisms (Double Log Spiral Wedges)

[64] The second and all the subsequent failures affect a region bordered by two log spirals (see Figure 3b). Six

Figure A1. Second failure mechanism in case of $\alpha \neq 0$. Gray lines are relative to the old spiral (B-C) whereas black lines to the new one (E-C). Dashed lines indicate the initial slope profile before first failure occurrence.

geometrical relationships may be established among the geometric variables ruling the shape of the two log spirals. In the following, the log spiral of the current slope profile and the log spiral of the failure line of the second (subsequent) mechanism will be denoted by the superscripts o (old) and n (new), respectively. These relationships may be easily derived by elementary geometric considerations:

$$r_y^n = r_x^n \exp[\tan \phi^n (y^n - x^n)], \quad (A6)$$

$$H = r_x^n \{\exp[\tan \phi^n (y^n - x^n)] \sin y^n - \sin x^n\}, \quad (A7)$$

$$L^n = r_x^n \{-\exp[\tan \phi^n (y^n - x^n)] \cos y^n + \cos x^n\}, \quad (A8)$$

$$r_y^o = r_x^o \exp[\tan \phi^o (y^o - x^o)], \quad (A9)$$

$$H = r_x^o \{\exp[\tan \phi^o (y^o - x^o)] \sin y^o - \sin x^o\}, \quad (A10)$$

and

$$L^o = r_x^o \{-\exp[\tan \phi^o (y^o - x^o)] \cos y^o + \cos x^o\}, \quad (A11)$$

where two different values of friction appear, ϕ^n and ϕ^o, since we are considering the case of both ϕ and c decrease. Therefore the value of friction at impending second (subsequent) failure is lower than the value at the occurrence of the first (previous) mechanism and so forth.

[65] Equation (4) is found by equating the external work done by the region B-C-E slipping away making a rigid rotation to the energy dissipated along the log spiral line E-C. The external work is calculated as the summation of many contributions, each of them expressing the work due to a different soil region. The rate of work done by the double logarithmic spiral shaped region B-C-E, area A^n, is obtained as the work done by the region P^n-C-E, area A_1^n, minus the work done by the regions P^n-D-E and P^n-D-C,

areas A_2^n and A_3^n, respectively, minus the work done by the region B-C-D (see Figure 3b). The last one is expressed again as the difference between the work done by region P^o-B-C, area A_1^o, and the two triangular regions P^o-D-B and P^o-D-C, areas A_2^o and A_3^n, respectively. Thus, the following equation is obtained:

$$\dot{W}_{ext} = \dot{W}_1^n - \dot{W}_2^n - \dot{W}_3^n - (\dot{W}_1^o - \dot{W}_2^o - \dot{W}_3^o). \quad (A12)$$

For sake of clarity, first the calculation of $\dot{W}_1^n$, $\dot{W}_2^n$, $\dot{W}_3^n$ will be shown and then of $\dot{W}_1^o$, $\dot{W}_2^o$, $\dot{W}_3^o$ In this case, the functions depend only on x^n, y^n (parameters of the new spiral n) and ϕ^n, the soil friction angle at the occurrence of the second landslide. So considering a differential element of region A_1 (see Figure A2), the rate of external work done by the soil weight is given by
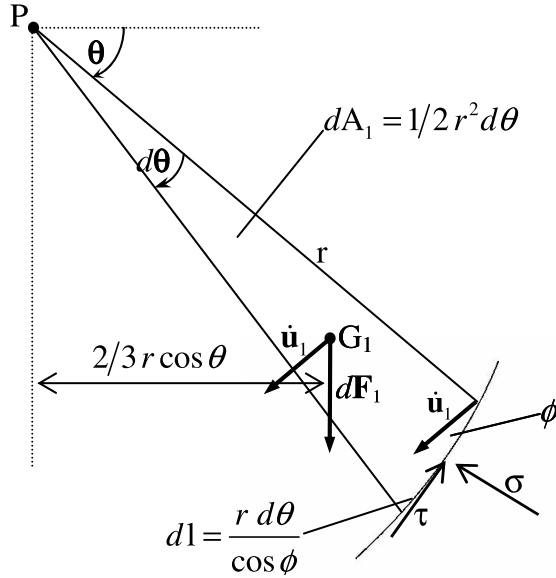
$$d\dot{W}_1^n = \dot{\mathbf{u}}_1^n \bullet d\mathbf{F}_1^n, \quad (A13)$$

where $\mathbf{u}_1$ is the displacement vector and $d\mathbf{F}_1 = -\gamma dA_1 \mathbf{k}$, with $\mathbf{k}$ vertical unit vector. Calculations lead to

$$d\dot{W}_1^n = |\dot{\mathbf{u}}_1^n| |d\mathbf{F}_1^n| \cos(\dot{\mathbf{u}}_1^n d\mathbf{F}_1^n)$$
$$= \dot{\omega} \frac{|X_{G_1} - X_P^n|}{\cos(\dot{\mathbf{u}}_1^n d\mathbf{F}_1^n)} \times \gamma dA_1^n \times \cos(\dot{\mathbf{u}}_1^n d\mathbf{F}_1^n) \quad (A14)$$
$$= \dot{\omega} \left(\frac{2}{3} r^n \cos \theta^n\right) \left(\gamma \frac{1}{2} (r^n)^2 d\theta^n\right).$$

After integrating over the entire area A_1^n, the work becomes

$$\dot{W}_1^n = \frac{1}{3} \dot{\omega} \gamma \int_{x^n}^{y^n} (r^n)^3 \cos \theta^n d\theta^n$$
$$= \frac{1}{3} \dot{\omega} \gamma (r_x^n)^3 \int_{x^n}^{y^n} \exp[3 \tan \phi^n (\theta^n - x^n)] \cos \theta^n d\theta^n. \quad (A15)$$

Figure A2. Differential element of either region A_1^o or A_1^n.

Integration by parts of the obtained expression leads to

$$\dot{W}_1^n = \dot{\omega}\gamma(r_x^n)^3 f_1(x^n, y^n, \phi^n), \tag{A16}$$

with the expression of $f_1(x, y, \phi)$ given in equation (A3).

[66] Considering now the area A_2^n, the rate of external work done by A_2^n is given by

$$\dot{W}_2^n = \dot{\mathbf{u}}_2^n \bullet \mathbf{F}_2^n = \dot{\omega}\frac{|X_{G_2} - X_{P^n}|}{\cos(\dot{\mathbf{u}}_2^n \mathbf{F}_2^n)} \times \gamma A_2^n \times \cos(\dot{\mathbf{u}}_2^n \mathbf{F}_2^n)$$
$$= \dot{\omega}\left[\frac{1}{3}\left(2r_x^n \cos x^n - L^n\right)\right]\left(\gamma\frac{1}{2}L^n r_x^n \sin x^n\right), \tag{A17}$$

and after some manipulations, using the geometrical relationships (A9) and (A10), it becomes

$$\dot{W}_2^n = \dot{\omega}\gamma(r_x^n)^3 f_2(x^n, y^n, \phi^n), \tag{A18}$$

where $f_2(x^n, y^n, \phi^n)$ is identical to equation (A4) when β is chosen equal to 90°. In this case the function simplifies to become

$$f_2(x^n, y^n, \phi^n) = \frac{1}{6}\sin x^n\{-\exp[2\tan\phi^n(y^n - x^n)] \\ \times (\cos y^n)^2 + (\cos x^n)^2\}. \tag{A19}$$

Considering the area A_3^n, the rate of external work done by A_3^n is given by

$$\dot{W}_3^n = \dot{\mathbf{u}}_3^n \bullet \mathbf{F}_3^n = \dot{\omega}\frac{|X_{G_3} - X_{P^n}|}{\cos(\dot{\mathbf{u}}_3^n \mathbf{F}_3)} \times \gamma A_3^n \times \cos(\dot{\mathbf{u}}_3^n \mathbf{F}_3^n)$$
$$= \dot{\omega}\left(\frac{2}{3}r_y^n \cos y^n\right)\left(\gamma\frac{1}{2}\mathrm{H}r_y^n \cos y^n\right), \tag{A20}$$

and after some manipulations, it becomes

$$\dot{W}_3^n = \dot{\omega}\gamma(r_x^n)^3 f_3(x^n, y^n, \phi^n), \tag{A21}$$

where $f_3(x^n, y^n, \phi^n)$ is identical to equation (A5) when β is chosen equal to 90°. In this case the function simplifies to become

$$f_3(x^n, y^n, \phi^n) = \frac{1}{3}\exp[2\tan\phi^n(y^n - x^n)](\cos y^n)^2 \\ \times \{\exp[\tan\phi^n(y^n - x^n)]\sin y^n + \sin x^n\}. \tag{A22}$$

Note that equations (A14), (A17), and (A20) may also have been achieved by calculating the moment of the considered soil regions, dA_1^n, A_2^n, A_3^n around point P^n.

[67] In a similar way, the areas of regions A_1^o, A_2^o, and A_3^o may be achieved. Considering, at first, the region A_1^o, whose gravity center is G_1, the rate of external work done by a differential element is (see Figure A2)

$$d\dot{W}_1^o = \dot{\mathbf{u}}_1^o \bullet d\mathbf{F}_1^o = \dot{\omega}\frac{|X_{G_1} - X_{P^n}|}{\cos(\dot{\mathbf{u}}_1^o d\mathbf{F}_1^o)} \times \gamma dA_1^o \times \cos(\dot{\mathbf{u}}_1^o d\mathbf{F}_1^o)$$
$$= \dot{\omega}\left(\frac{2}{3}r^o \cos\theta^o - r_y^o \cos y^o + r_y^n \cos y^n\right)\left(\gamma\frac{1}{2}(r^o)^2 d\theta^o\right), \tag{A23}$$

where $\dot{\mathbf{u}}_1^o$ is the displacement vector, $d\mathbf{F}_1^o = -\gamma dA_1^o\mathbf{k}$, with $\mathbf{k}$ vertical unit vector, and $\dot{\omega}$ is the rate of angular displacement of the infinitesimal element. Therefore, the external work for the entire region becomes

$$\dot{W}_1^o = \dot{\omega}\frac{1}{3}\gamma\left[\left(-\frac{3}{2}r_y^o \cos y^o + \frac{3}{2}r_y \cos y\right) \\ \times \int_{x^o}^{y^o}(r^o)^2 d\theta^o + \int_{x^o}^{y^o}(r^o)^3 \cos\theta^o d\theta^o\right], \tag{A24}$$

and, after integration by parts,

$$\dot{W}_1^o = \dot{\omega}\frac{1}{3}\gamma\left[\left(-\frac{3}{2}r_y^o \cos y^o + \frac{3}{2}r_y^n \cos y^n\right)(r_x^o)^2\frac{\exp(2\tan\phi^o(y^o - x^o)) - 1}{2\tan\phi^o} + \\ + (r_x^o)^3\frac{\exp(3\tan\phi^o(y^o - x^o))(\sin y^o + 3\tan\phi^o \cos y^o) - (\sin x^o + 3\tan\phi^o \cos x^o)}{1 + 9(\tan\phi^o)^2}\right]. \tag{A25}$$

Substituting equations (A6), (A7), (A9), and (A10) into equation (A25) leads to

$$
\dot{W}_1^o = \dot{\omega}\gamma\left(r_x^n\right)^3 m_1(x^n, y^n, \phi^n, x^o, y^o, \phi^o) \text{ with}
$$

$$
m_1 = \left(\frac{r_x^o}{r_x^n}\right)^2 \frac{\exp[\tan\phi(y-x)]\cos y(\exp(2\tan\phi^o(y^o-x^o))-1)}{4\tan\phi^o} +
$$

$$
+ \left(\frac{r_x^o}{r_x^n}\right)^3 \left[\frac{\exp(3\tan\phi^o(y^o-x^o))(\sin y^o + 3\tan\phi^o\cos y^o) - (\sin x^o + 3\tan\phi^o\cos x^o)}{3\left(1+9(\tan\phi^o)^2\right)} + \right.
$$

$$
\left. - \frac{\exp[\tan\phi^o(y^o-x^o)]\cos y^o(\exp(2\tan\phi^o(y^o-x^o))-1)}{4\tan\phi^o}\right]
$$

(A26)

and

$$
\frac{r_x^o}{r_x^n} = \frac{\exp[\tan\phi^n(y^n-x^n)]\sin y^n - \sin x^n}{\exp[\tan\phi^o(y^o-x^o)]\sin y^o - \sin x^o}.
$$

(A27)

Considering now the region A_2^o, whose gravity center is G_2, the rate of external work is given by

$$
\dot{W}_2^o = \dot{\mathbf{u}}_2^o \bullet \mathbf{F}_2^o = \dot{\omega}\frac{|\mathbf{X}_{G_2} - \mathbf{X}_{P^n}|}{\cos\left(\dot{\mathbf{u}}_2^o\mathbf{F}_2^o\right)} \times \gamma A_2^o \times \cos\left(\dot{\mathbf{u}}_2^o\mathbf{F}_2^o\right)
$$

$$
= \dot{\omega}\left(-r_y^o\cos y^o + \frac{1}{3}\left(2r_x^o\cos x^o - L^o\right) + r_y\cos y\right)\left(\gamma\frac{1}{2}L^o r_x^o\sin x^o\right).
$$

(A28)

After some manipulations and substituting equations (A6), (A7), (A9), and (A10), into equation (A28), the following expression is obtained:

$$
\dot{W}_2^o = \dot{\omega}\gamma\left(r_x^n\right)^3 m_2(x^n, y^n, \phi^n, x^o, y^o, \phi^o) \text{ with}
$$

$$
m_2 = \frac{1}{2}\left(\frac{r_x^o}{r_x^n}\right)^2\frac{L^o}{r_x^o}\sin x^o\left[\exp(\tan\phi^n(y^n-x^n))\cos y^n\right.
$$

$$
\left. + \frac{1}{3}\frac{r_x^o}{r_x^n}\left(2\cos x^o - \frac{L^o}{r_x^o} - 3\exp(\tan\phi^o(y^o-x^o))\cos y^o\right)\right]
$$

(A29)

and L^o/r_x^o given in equation (A11).

[68] Considering now the region A_3^o, whose gravity center is G_3, the rate of external work is given by

$$
\dot{W}_3^o = \dot{\mathbf{u}}_3^o \bullet \mathbf{F}_3^o = \dot{\omega}\frac{|\mathbf{X}_{G_3} - \mathbf{X}_{P^n}|}{\cos\left(\dot{\mathbf{u}}_3^o\mathbf{F}_3^o\right)} \times \gamma A_3^o \times \cos\left(\dot{\mathbf{u}}_3^o\mathbf{F}_3^o\right)
$$

$$
= \dot{\omega}\left(r_y^n\cos y^n - \frac{1}{3}r_y^o\cos y^o\right)\left(\gamma\frac{1}{2}H r_y^o\cos y^o\right).
$$

(A30)

After some manipulations and substituting equations (A7) and (A10), into equation (A30), the following expression is obtained:

$$
\dot{W}_3^o = \dot{\omega}\gamma\left(r_x^n\right)^3 m_3(x^n, y^n, \phi^n, x^o, y^o, \phi^o) \text{ with}
$$

$$
m_3 = \frac{1}{2}\left(\frac{r_x^o}{r_x^n}\right)^2[\exp(\tan\phi^o(y^o-x^o))\sin y^o + \sin x^o]
$$

$$
\times \exp(\tan\phi^o(y^o-x^o))\cos y^o \times \left\{\exp(\tan\phi^n(y^n-x^n))\cos y^n + \right.
$$

$$
\left. - \frac{1}{3}\frac{r_x^o}{r_x^n}[\exp(\tan\phi^o(y^o-x^o))\cos y^o]\right\}.
$$

(A31)

Note that equations (A23), (A28), and (A30) may also have been achieved by calculating the moment of the considered soil regions, dA_1^o, A_2^o, A_3^o around point P^n.

[69] The last contribution to be calculated is the internal work. All energy dissipation occurs along the logarithmic spiral E-C. The rate of energy dissipation along a differential element of the spiral is (see Figure A2)

$$
d\dot{W}_d = (\sigma\dot{\varepsilon} + \tau\dot{\gamma})dl.
$$

(A32)

According to the associated flow rule $\dot{\varepsilon} = -\dot{\gamma}\tan\phi^n$, therefore substituting this expression into equation (A32) leads to:

$$
d\dot{W}_d = [-\sigma\dot{\gamma}\tan\phi^n + (\sigma\tan\phi^n + c)\dot{\gamma}]\frac{r^n d\theta^n}{\cos\phi^n}
$$

$$
= c \times \dot{\omega}r^n\cos\phi^n \times \frac{r^n d\theta^n}{\cos\phi^n} = c\dot{\omega}(r^n)^2 d\theta^n.
$$

(A33)

Hence the total rate of energy dissipation is

$$
\dot{W}_d = \dot{\omega}c\int_{x^n}^{y^n}(r^n)^2 d\theta^n,
$$

(A34)

which after integration becomes

$$
\dot{W}_d = \dot{\omega}c\left(r_x^n\right)^2\frac{\exp[2\tan\phi^n(y^n-x^n)]-1}{2\tan\phi^n}.
$$

(A35)

From equations (1) and (A12) it follows that

$$
\dot{W}_1^n - \dot{W}_2^n - \dot{W}_3^n - \dot{W}_1^o + \dot{W}_2^o + \dot{W}_3^o = \dot{W}_d.
$$

(A36)

Now equations (A16), (A18), (A21), (A26), (A29), and (A31) may be substituted into equation (A36). All the terms in equation (A36) contain $\dot{\omega}$ and $(r_x^n)^2$ which therefore may be simplified. After rearranging, equation (A36) becomes

$$
\gamma r_x^n(f_1 - f_2 - f_3 - m_1 + m_2 + m_3) = c\frac{\exp[\tan\phi^n(y^n-x^n)]-1}{2\tan\phi^n},
$$

(A37)

and then rearranging

$$
c = \frac{\gamma H}{g(x^n, y^n, \phi^n, x^o, y^o, \phi^o)} \text{ with}
$$

$$
g = \frac{\{\exp[\tan\phi^n(y^n-x^n)]\sin y^n - \sin x^n\}\{\exp[2\tan\phi^n(y^n-x^n)]-1\}}{2\tan\phi^n(f_1 - f_2 - f_3 - m_1 + m_2 + m_3)}.
$$

(A38)

The value of cohesion at failure is given by

$$c = \frac{\gamma H}{\min_{x^n, y^n} g(x^n, y^n, \phi^n, x^o, y^o, \phi^o)} = \frac{\gamma H}{N_S}. \qquad (A39)$$

Note that the function g is a two variable function with the values of the 4 parameters ϕ^n, x^o, y^o, ϕ^o known and constant; therefore the domain involved in the search for the minimum of the function is a 2-D one. Initially the Matlab command fminsearch was used to look for the minimum. This algorithm works in some cases, but in some other cases and most of the times in the more complex case of $\alpha \neq 0$ the minimum achieved by the optimization algorithm might be very far from the real one. This is due to the mathematical structure of the function. In fact, the function is composed of many products of transcendental expressions, for example, $\exp(\tan\phi(y - x))$, with trigonometric functions, for example, $\sin(x)$, which cause the function to oscillate between positive and negative along several asymptotes. In more lay terms, the function can be seen as made by several long and low steep valleys transversally bordered by very steep ascents. This makes the use of standard optimization algorithms particularly difficult since an unlucky choice of the starting point for the algorithm searching the minimum could lead to a very inaccurate result especially in terms of location of the minimum point (x, y) which governs the geometry of the failure mechanism and therefore leading to the assumption of a completely wrong failure line. Fortunately, the function is available in an explicit form and depends only on two variables; therefore in order to carry out a parametric analysis (see Figure 19 and Table 2) the minimum was calculated simply by evaluating the function over a sufficiently fine grid of x, y points within a physically admissible domain; then taking the positive lowest value among all the evaluated points. See funI_evalnum, funM_evalnum, funIalfa_evalnum, funMalfa_evalnum, and funTalfa_evalnum in the auxiliary material. Finally the formulas used for the calculation of the areas of the detaching soil masses can be found in the Matlab files reported in the auxiliary material as well.

Notation

α inclination of the slope summit.
β initial inclination of a straight slope/cliff.
γ unit weight.
γ' submerged unit weight.
$\dot{\gamma}$ angular strain rate.
$\dot{\varepsilon}$ normal strain rate.
ζ scree inclination.
θ, θ^o generic logarithmic spiral angle.
λ inclination of the linear envelope.
ρ particle radii scaling factor for DEM simulations.
σ normal stress.
τ shear stress.
ϕ internal friction angle.
ϕ_μ micromechanical friction angle.
Ψ dilation angle.

$\dot{\omega}$ rotation rate.
a acceleration.
c cohesion.
c_μ micromechanical cohesion.
d bulking ratio.
h height of part of the slope.
k_1, k_2, k_3, k_4 constant coefficients.
l arc length as defined in Figure A2.
l_1, l_2 lengths.
l_3, l_4 lengths.
m mass.
n porosity.
r radius of curvature.
r_x^n minimum radius of curvature of the logarithmic spiral of the current failure mechanism.
r_x^o minimum radius of curvature of the old (previous failure) logarithmic spiral.
r_y^n maximum radius of curvature of the logarithmic spiral of the current failure mechanism.
r_y^o maximum radius of curvature of the old (previous failure) logarithmic spiral.
s slope gradient.
t time.
t_μ micromechanical tensile strength.
$\mathbf{u}$ displacement vector.
v, v_D, v_k velocities.
x^n minimum angle of the logarithmic spiral of the current failure mechanism.
x^o minimum angle of the old (previous failure) logarithmic spiral.
y^n maximum angle of the logarithmic spiral of the current failure mechanism.
y^o maximum angle of the old (previous failure) logarithmic spiral.
A area.
$A^n, A_1^n, A_2^n, A_3^n,$ A^o, A_1^o, A_2^o, A_3^o areas of the regions defined in Figure 3b.
C time scaling constant factor for DEM simulations.
CR crest retreat.
D damage index.
$F^n, F_1^n, F_2^n, F_3^n,$ F^o, F_1^o, F_2^o, F_3^o gravity forces acting on the corresponding regions A^n, etc.
F_k generic force on a particle.
F^N normal contact force between two particles.
F^S shear contact force between two particles.
G gravity center.
H height of full slope.
L^n, L^o lengths defined in Figure 3b.
N_S stability number.
X horizontal Cartesian coordinate; axes origin at the initial slope toe.
Y vertical Cartesian coordinate; axes origin at the initial slope toe.
W work.
$\dot{W}^n, \dot{W}_1^n, \dot{W}_2^n, \dot{W}_3^n,$ $\dot{W}^o, \dot{W}_1^o, \dot{W}_2^o, \dot{W}_3^o$ external work rates done by the corresponding regions A^n, etc.

References

Ahnert, F. (1970a), Brief description of a comprehensive three-dimensional process-response model of landform development, *Z. Geomorphol. Suppl.*, 24, 11–22.

Ahnert, F. (1970b), A comparison of theoretical slope models with slopes in the field, *Z. Geomorphol. Suppl.*, 9, 88–101.

Ahnert, F. (1970c), Functional relationships between denudation, relief and uplift in large mid-latitude drainage basins, *Am. J. Sci.*, 268, 243–263, doi:10.2475/ajs.268.3.243.

Anderson, R. S., and N. F. Humphrey (1989). Interaction of weathering and transport processes in the evolution arid landscapes, in *Quantitative Dynamic Stratigraphy*, edited by T. A. Cross, pp. 349–361, Prentice Hall, Englewood Cliffs, N. J.

Anderson, S. P., W. E. Dietrich, and G. H. Brimhall (2002), Weathering profiles, mass-balance analysis, and rates of solute loss: Linkages between weathering and erosion in a small, steep catchment, *Geol. Soc. Am. Bull.*, 114(9), 1143–1158.

Andrews, D. J., and R. C. Bucknam (1987), Fitting degradation of shoreline scarps by a nonlinear diffusion model, *J. Geophys. Res.*, 92(B12), 12,857–12,867, doi:10.1029/JB092iB12p12857.

Bakker, J. P., and J. W. N. Le Heux (1946), Projective-geometric treatment of O. Lehmann's theory of the transformation of steep mountain slopes, *Proc. K. Ned. Akad. Wet.*, 49, 533–547.

Bakker, J. P., and J. W. N. Le Heux (1952), A remarkable new geomorphological law, *Proc. K. Ned. Akad. Wet., Ser. B*, 55, 399–410, 554–571.

Bekaert, A. (1995), Improvement of the kinematic bound for the stability of a vertical cut-off, *Mech. Res. Commun.*, 22, 533–540, doi:10.1016/0093-6413(95)00058-5.

Carson, M. A., and M. J. Kirkby (1972), *Hillslope Form and Process*, 475 pp., Cambridge Univ. Press, Cambridge, U. K.

Chase, C. G. (1992), Fluvial landsculpting and the fractal dimension of topography, *Geomorphology*, 5, 39–57, doi:10.1016/0169-555X(92)90057-U.

Chen, W. F. (1975), *Limit Analysis and Soil Plasticity*, Elsevier, Amsterdam.

Colman, S. M., and K. Watson (1983), Ages estimated from a diffusion equation model for scarp degration, *Science*, 221, 263–265, doi:10.1126/science.221.4607.263.

Culling, W. E. H. (1963), Soil creep and the development of hillside slopes, *J. Geol.*, 71, 127–161.

Dawson, E. M., W. H. Roth, and A. Drescher (1999), Slope stability analysis by strength reduction, *Geotechnique*, 49, 835–840, doi:10.1680/geot.1999.49.6.835.

Dietrich, W. E., D. G. Bellugi, L. S. Sklar, J. D. Stock, A. M. Heimsath, and J. J. Roering (2003), Geomorphic transport laws for predicting landscape form and dynamics, in *Prediction in Geomorphology*, *Geophys. Monogr. Ser.*, vol. 135, edited by P. Wilcock and R. Iverson, pp. 103–132, AGU, Washington, D.C., doi:10.1029/135GM09.

Fernandes, N. F., and W. E. Dietrich (1997), Hillslope evolution by diffusive processes: The timescale for equilibrium adjustments, *Water Resour. Res.*, 33(6), 1307–1318, doi:10.1029/97WR00534.

Fisher, O. (1866), On the disintegration of a chalk cliff, *Geol. Mag.*, 3, 354–356, doi:10.1017/S0016756800167573.

Fredlund, D. G., and H. Rahardjo (1993), *Soil Mechanics for Unsaturated Soils*, 517 pp., Wiley, New York.

Gostelow, T. P. (1974), Slope development in stiff overconsolidated clays, Ph.D thesis, Imperial College, Univ. of London, London.

Hachinohe, S., N. Hiraki, and T. Suzuki (2000), Rates of weathering and temporal changes in strength of bedrock of marine terraces in Boso Peninsula, Japan, *Eng. Geol. Amsterdam*, 55, 29–43, doi:10.1016/S0013-7952(99)00104-0.

Hanks, T. C., and D. J. Andrews (1989), Effect of far-field slope on morphologic dating of scarplike landforms, *J. Geophys. Res.*, 94(B1), 565–573, doi:10.1029/JB094iB01p00565.

Hanks, T. C., R. C. Bucknam, and K. R. Lajoie (1984), Modification of wave-cut and faulting controlled landforms, *J. Geophys. Res.*, 89(B7), 5771–5790, doi:10.1029/JB089iB07p05771.

Heimsath, A. M., W. E. Dietrich, K. Nishiizumi, and R. C. Finkel (1997), The soil production function and landscape equilibrium, *Nature*, 388, 358–361, doi:10.1038/41056.

Howard, A. D. (1994), A detachment-limited model of drainage basin evolution, *Water Resour. Res.*, 30, 2261–2285, doi:10.1029/94WR00757.

Hutchinson, J. N. (1973), The response of London Clay cliffs to differing rates of toe erosion, *Geol. Appl. Idrogeol.*, 7, 221–239.

Hutchinson, J. N. (2001), Reading the ground: Morphology and geology in site appraisal, *Q. J. Eng. Geol. Hydrogeol.*, 34, 7–50, doi:10.1144/qjegh.34.1.7.

Kimmance, G. C. (1988), Computer aided risk analysis of open pit mine slopes in kaolin mined deposits, Ph.D thesis, Univ. of London, London.

Kirkby, M. J. (1971), Hillslope process-response models based on the continuity equation, in *Slopes, Form and Process*, *Inst. Br. Geogr. Spec. Pub.*, vol. 3, edited by D. Brunsden, pp. 15–30, Inst. of Br. Geogr., London.

Kirkby, M. J. (1987), General models of long-term slope evolution through mass movement, in *Slope Stability*, edited by M. G. Anderson and K. S. Richards, pp. 359–379, John Wiley, New York.

Kooi, H., and C. Beaumont (1994), Escarpment evolution on high-elevation rifted margins: Insights derived from a surface processes model that combines diffusion, advection, and reaction, *J. Geophys. Res.*, 99(B6), 12,191–12,209, doi:10.1029/94JB00047.

Koons, P. O. (1989), The topographic evolution of collisional mountain belts: A numerical look at the Southern Alps, New Zealand, *Am. J. Sci.*, 289, 1041–1069, doi:10.2475/ajs.289.9.1041.

Lehmann, O. (1933), Morphologische Theorie der Verwitterung von SteinschlagwÄanden, *Vierteljahresschr. Naturforsch. Ges. Zurich*, 78, 83–126.

Leroueil, S., and P. R. Vaughan (1990), The general and congruent effects of structure in natural soils and weak rocks, *Geotechnique*, 40, 467–488, doi:10.1680/geot.1990.40.3.467.

Lyamin, A. V., and S. W. Sloan (2002), Lower bound limit analysis using non-linear programming, *Int. J. Numer. Methods Eng.*, 55, 573–611, doi:10.1002/nme.511.

Marques, E. A. G., E. V. Barroso, A. P. Menezes Filho, and E. do A. Vargas Jr. (2010), Weathering zones on metamorphic rocks from Rio de Janeiro—Physical, mineralogical and geomechanical characterization, *Eng. Geol. Amsterdam*, 111, 1–18, doi:10.1016/j.enggeo.2009.11.001.

Martin, Y. (2000), Modelling hillslope evolution: Linear and non linear transport relations, *Geomorphology*, 34, 1–21, doi:10.1016/S0169-555X(99)00127-0.

Martin, Y., and M. Church (1997), Diffusion in landscape development models: On the nature of basic transport relations, *Earth Surf. Processes Landforms*, 22(3), 273–279, doi:10.1002/(SICI)1096-9837(199703)22:3<273::AID-ESP755>3.0.CO;2-D.

Martin, Y., and M. Church (2004), Numerical modelling of landscape evolution: Geomorphological perspectives, *Prog. Phys. Geogr.*, 28(3), 317–339, doi:10.1191/0309133304pp412ra.

Michalowski, R. (2002), Stability charts for uniform slopes. ASCE, *J. Geotech. Geoenviron. Eng.*, 128, 351–355, doi:10.1061/(ASCE)1090-0241(2002)128:4(351).

Nash, D. B. (1980a), Forms of bluffs degraded for different lengths of time in Emmet County, Michigan, U.S.A, *Earth Surf. Processes*, 5, 331–345, doi:10.1002/esp.3760050405.

Nash, D. B. (1980b), Morphologic dating of degraded normal fault scarps, *J. Geol.*, 88, 353–360, doi:10.1086/628513.

Pelletier, J. D., S. B. DeLong, A. H. Al-Suwaidi, M. Cline, Y. Lewis, J. L. Psillas, and B. Yanites (2006), Evolution of the Bonneville shoreline scarp in west-central Utah: Comparison of scarp-analysis methods and implications for the diffusions model of hillslope evolution, *Geomorphology*, 74(1–4), 257–270, doi:10.1016/j.geomorph.2005.08.008.

Pierce, K. L., and S. M. Colman (1986), Effect of height and orientation (microclimate) on geomorphic degradation rate and processes, late glacial terrace scarps in central Idaho, *Geol. Soc. Am. Bull.*, 97, 869–885, doi:10.1130/0016-7606(1986)97<869:EOHAOM>2.0.CO;2.

Radenkovic, D. (1961), Théorie des charges limites: Extension à la mécanique des sols, *Publ. Sci. Tech. Minist. Air (Fr.)*, 116.

Rao, S. M. (1996), Role of apparent cohesion in the stability of Dominican allophane soil slopes, *Eng. Geol. Amsterdam*, 43, 265–279, doi:10.1016/S0013-7952(96)00036-1.

Roering, J. J., J. W. Kirchner, and W. E. Dietrich (1999), Evidence for nonlinear, diffusive sediment transport on hillslopes and implications for landscape morphology, *Water Resour. Res.*, 35(3), 853–870, doi:10.1029/1998WR900090.

Roering, J. J., J. W. Kirchner, and W. E. Dietrich (2001a), Hillslope evolution by nonlinear, slope-dependent transport: Steady state morphology and equilibrium adjustment timescales, *J. Geophys. Res.*, 106, 16,499–16,513, doi:10.1029/2001JB000323.

Roering, J. J., J. W. Kirchner, L. S. Sklar, and W. E. Dietrich (2001b), Hillslope evolution by nonlinear creep and landsliding: An experimental study, *Geology*, 29(2), 143–146, doi:10.1130/0091-7613(2001)029<0143:HEBNCA>2.0.CO;2.

Scheidegger, A. E. (1961), Mathematical models of slope development, *Geol. Soc. Am. Bull.*, 72, 37–50, doi:10.1130/0016-7606(1961)72[37:MMOSD]2.0.CO;2.

Shield, R. T., and D. C. Drucker (1953), The application of limit analysis to punch indentation problems, *J. Appl. Mech.*, *20*, 453–460.

Taylor, D. W. (1948), *Fundamentals of Soil Mechanics*, John Wiley, New York.

Utili, S. (2005), An analytical relationship for weathering induced slope retrogression: A benchmark, *Ital. Geotech. J.*, *39*(2), 9–30.

Utili, S. (2006), Evolution of natural slopes subject to weathering: An analytical and numerical study, Ph.D thesis, Politecnico di Milano, Milan, Italy.

Utili, S., and G. B. Crosta (2011), Modeling the evolution of natural cliffs subject to weathering: 2. Discrete element approach, *J. Geophys. Res.*, *116*, F01017, doi:10.1029/2009JF001559.

Utili, S., and R. Nova (2007), On the optimal profile of a slope, *Soil Found.*, *47*, 717–729.

Utili, S., and R. Nova (2008), DEM analysis of bonded granular geomaterials, *Int. J. Numer. Anal. Methods Geomech.*, *32*, 1997–2031, doi:10.1002/nag.728.

Viratjandr, C., and R. L. Michalowski (2006), Limit analysis of submerged slopes, *Can. Geotech. J.*, *43*, 802–814, doi:10.1139/T06-042.

Wallace, R. E. (1980), Degradation of the Hegben Lake fault scarps of 1959, *Geology*, *8*, 225–229, doi:10.1130/0091-7613(1980)8<225: DOTHLF>2.0.CO;2.

Wang, Y. H., and S. C. Leung (2008), Characterization of cemented sand by experimental and numerical investigations, *J. Geotech. Geoenviron. Eng.*, *134*, 992–1004, doi:10.1061/(ASCE)1090-0241(2008)134:7(992).

White, A. F., and S. L. Brantley (2003), The effect of time on the weathering of silicate minerals: Why do weathering rates differ in the laboratory and field?, *Chem. Geol.*, *202*(3–4), 479–506, doi:10.1016/j.chemgeo.2003.03.001.

White, A. F., M. S. Schulz, D. V. Vivit, A. E. Blum, D. A. Stonestrom, and S. P. Anderson (2008), Chemical weathering of a marine terrace chronosequence, Santa Cruz, California I: Interpreting rates and controls based on soil concentration-depth profiles, *Geochim. Cosmochim. Acta*, *72*, 36–68, doi:10.1016/j.gca.2007.08.029.

White, A. F., M. S. Schulz, D. A. Stonestrom, D. V. Vivit, J. Fitzpatrick, T. D. Bullen, K. Maher, and A. E. Blum (2009), Chemical weathering of a marine terrace chronosequence, Santa Cruz, California. Part II: Solute profiles, gradients and the comparisons of contemporary and long-term weathering rates, *Geochim. Cosmochim. Acta*, *73*, 2769–2803, doi:10.1016/j.gca.2009.01.029.

Willgoose, G., R. Bras, and I. Rodriguez-Iturbe (1991), Results from a new model of river basin evolution, *Earth Surf. Processes Landforms*, *16*, 237–254, doi:10.1002/esp.3290160305.

Yokota, S., and A. Iwamatsu (2000), Weathering distribution in a steep slope of soft pyroclastic rocks as an indicator of slope instability, *Eng. Geol. Amsterdam*, *55*, 57–68, doi:10.1016/S0013-7952(99)00106-4.

Zheng, H., D. F. Liu, and C. G. Li (2005), Slope stability analysis based on elasto-plastic finite element method, *Int. J. Numer. Methods Eng.*, *64*, 1871–1888, doi:10.1002/nme.1406.

Zhu, M., and R. L. Michalowski (2005), Shape factors for limit loads on square and rectangular footings, *J. Geotech. Geoenviron. Eng.*, *131*, 223–231, doi:10.1061/(ASCE)1090-0241(2005)131:2(223).

G. B. Crosta, Dipartimento di Scienze Geologiche e Geotecnologie, Università degli Studi di Milano-Bicocca, Piazza della Scienza 4, Milano I-20126, Italy.

S. Utili, Department of Engineering Science, University of Oxford, Parks Road, Jenkin Bldg., Rm. 21, Oxford OX1 3PJ, UK. (stefano.utili@eng.ox. ac.uk)